

Magnetoconvection in a horizontal duct flow at very high Hartmann and Grashof numbers

R. Akhmedagaev¹, O. Zikanov^{1†}, and Y. Listratov^{2,3}

¹University of Michigan - Dearborn, 4901 Evergreen Road, Dearborn, MI 48128-1491, USA

²Moscow Power Engineering Institute, 14 Krasnokazarmennaya Street, Moscow, 111250, Russia

³Joint Institute for High Temperatures Russian Academy of Science, Izhorskaya Street 13, Building 2, Moscow, 125412, Russia

Direct numerical simulations and linear stability analysis are carried out to study mixed convection in a horizontal duct with constant-rate heating applied at the bottom and imposed transverse horizontal magnetic field. A two-dimensional approximation corresponding to the asymptotic limit of very strong magnetic field effect is validated and applied, together with full three-dimensional analysis, to investigate the flow's behaviour in the previously unexplored range of control parameters corresponding to typical conditions of a liquid metal blanket of a nuclear fusion reactor. It is found that the instability to quasi-two-dimensional rolls parallel to the magnetic field discovered at smaller Hartmann and Grashof numbers in earlier studies also occurs in this parameter range. Transport of the rolls by the mean flow leads to magnetoconvective temperature fluctuations of exceptionally high amplitudes. It is also demonstrated that quasi-two-dimensional structure of flows at very high Hartmann numbers does not guarantee accuracy of the classical two-dimensional approximation. The accuracy deteriorates at the highest Grashof numbers considered in the study.

1. Introduction

Combined convection and magnetohydrodynamic (MHD) effects dramatically change the nature of flows of electrically conducting fluids. The combination appears in many technological applications such as metallurgy, liquid metal batteries, and growth of semiconductor crystals (Ozoe 2005; Davidson 2016). Another prominent example is the liquid metal blankets of nuclear fusion reactors where an electrically conducting fluid (e.g., a PbLi alloy) serves as a coolant, radiation shield and tritium breeder (Abdou *et al.* 2015). A distinctive feature of this system is that the convection and magnetic field effects are both exceptionally strong.

Many aspects of the transformation of flows of electrically conducting fluid under the influence of a strong magnetic field, such as suppression of turbulent fluctuations, anisotropic or quasi-two-dimensional (Q2D) states with zero or weak velocity gradients along the field lines, formation of MHD boundary layers, and delay of laminar-turbulent transition, are relatively well understood (see, e.g., Branover 1978; Davidson 2016; Sommeria & Moreau 1982; Zikanov *et al.* 2014). This paper addresses a recently discovered and still poorly understood phenomenon - the high amplitude fluctuations in flows in ducts and pipes (see, e.g., Genin *et al.* 2011; Vetcha *et al.* 2013; Zikanov *et al.* 2013; Belyaev *et al.* 2021). The term magneto-convective fluctuations (MCFs) proposed for the phenomenon by Belyaev *et al.* (2021) will be used in this paper. As discussed in detail in the review of Zikanov *et al.* (2021) and references therein, the fluctuations have been detected in experimental and computational studies of a large variety of systems: pipes

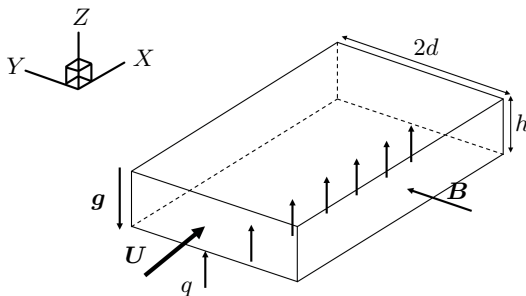


FIGURE 1. Flow geometry and coordinate system. The arrows marked by letters g , B and q denote, respectively, the orientations of the gravity acceleration, magnetic field and wall heating.

and ducts of various orientations with respect to gravity, various heating arrangements, and various configurations of the magnetic field.

The nature of the magnetoconvective fluctuations can be briefly described as follows. They appear in the conditions of a very strong magnetic field effect, i.e. in the range of Hartmann numbers, where turbulence is fully suppressed by magnetic damping. In experiments, the MCFs are manifested by oscillations of temperature with very high amplitude (up to $50K$ in some cases) and typical frequencies much lower than the frequencies of turbulence-induced fluctuations. Specific properties of the MCFs vary with the flow's configuration and values of the control parameters (Zikanov *et al.* 2021). The effect has potentially serious consequences for design and operation of liquid metal blankets of future fusion reactors. Should the fluctuations appear in an actual blanket, they will lead to strong and unsteady thermal stresses in the walls. Due to their possibly very large amplitude, the stresses will threaten the structural integrity of a fusion reactor system. Significant effects on heat transfer, transport of tritium, and wall corrosion are also anticipated. As we discuss later in this section, it is yet impossible to say how realistic these expectations are, since no experiments or computations at very high Ha and Gr typical for reactor conditions have been conducted so far.

Flows in a rectangular duct with heating applied at the bottom and imposed transverse horizontal magnetic field (see figure 1) are considered in this paper. The configuration is relevant to design of blankets and divertors of fusion reactors (Kirillov & Muraviev 1997). It is also important as an archetypal system, in which the MCFs were first identified (in Genin *et al.* (2011) and Zikanov *et al.* (2013), where they were named anomalous fluctuations) and explained.

Similar systems for either ducts or round pipes have been studied experimentally (Genin *et al.* 2011; Belyaev *et al.* 2015; Sahu *et al.* 2020) and numerically (Zikanov *et al.* 2013; Zhang & Zikanov 2014; Vo *et al.* 2017; Listratov *et al.* 2018). The flow is controlled by four dimensionless parameters: the Reynolds, Prandtl, Grashof and Hartmann numbers,

$$Re = \frac{Ud}{\nu}, \quad Pr = \frac{\nu}{\chi}, \quad Gr = \frac{g\beta qd^4}{\nu^2\kappa}, \quad Ha = Bd\sqrt{\frac{\sigma}{\rho\nu}}, \quad (1.1)$$

with the duct half-width d , the mean streamwise velocity U , the kinematic viscosity ν , the temperature diffusivity χ , the acceleration due to gravity g , the coefficient of thermal expansion β , the heat flux of constant rate q , the thermal conductivity κ , the electrical conductivity σ and the mass density ρ . Rectangular duct geometry adds the aspect ratio $\Gamma = 2d/h$ as a parameter, where h is the height of the duct.

Interesting results were obtained in the linear stability analysis of the Poiseuille-Rayleigh-Bénard duct flow with a transverse magnetic field performed by Vo *et al.*

(2017). Two-dimensional approximation valid in the limit of strong magnetic field presented later in this paper was used. One important result of Vo *et al.* (2017) is relevant to our work even though different boundary conditions were used. It was demonstrated that the convection instability occurs at moderate and high Grashof number (approximately above 10^6) at the Hartmann numbers ($\sim 10^4$) typical for reactor blanket conditions.

The presence of MCFs in a horizontal round pipe with a lower half of the wall heated was detected in experiments (Genin *et al.* 2011; Belyaev *et al.* 2015) and explained in the linear stability analysis and direct numerical simulations (DNS) by Zikanov *et al.* (2013). Flows of mercury with $Pr \approx 0.022$, Re up to 10^5 , Gr up to 10^8 , and Ha up to 500 were investigated. It was shown that at a strong magnetic field the suppression of flow structures having large gradients along the field lines resulted in the most unstable modes in the form of convection rolls with axes aligned with the field. The instability led to development of convection structures in the form of Q2D rolls. Transport of the rolls by the mean flow generated the MCFs.

The analysis was extended in the numerical simulations of Zhang & Zikanov (2014). Flows in a horizontal duct of aspect ratio $\Gamma = 1$ with bottom heating and transverse magnetic field at $Pr = 0.0321$, $Re = 5000$, $50 \leq Ha \leq 800$ and $10^5 \leq Gr \leq 10^9$ were investigated. The instability leading to the formation of Q2D rolls similar to those found in the pipe flow was detected at sufficiently high Gr and Ha .

Investigations of Zhang & Zikanov (2014) conducted in the broader range of parameters than for the pipe flow demonstrated existence of two distinct secondary flow regimes. The realization of the regimes depended on the relative strength of the convection and MHD effects. The low- Gr type characterized by Q2D distributions of velocity and temperature dominated by spanwise rolls appeared at Gr below a certain $Gr^*(Ha)$. At higher Gr , stronger convection resulted in three-dimensional (3D) flow states combining the spanwise rolls with streamwise ones (the geometrically preferred convection structure in pipes and ducts with bottom heating).

Flows of liquid metals in fusion reactor blankets and divertors are subject to very strong effects of convection ($Gr \sim 10^{10} - 10^{12}$) and magnetic fields ($Ha \sim 10^4$) (see, e.g., Smolentsev *et al.* 2008, 2010). Such extreme parameters present serious obstacles to analysis, because neither laboratory experiments nor 3D simulations of unsteady flow regimes in realistic blanket or divertor geometries can, at this moment, achieve such values.

In an attempt to reach the typical blanket flow conditions, the data on two types of the secondary flow regime in a horizontal duct were extrapolated to high Gr and Ha by Zhang & Zikanov (2014). The extrapolation predicted existence of MCFs at the typical blanket parameters. It also predicted that the flow would likely be of the low- Gr type at $Gr \leq 10^{10}$ and of the high- Gr type at higher Gr . The experiments in the pipe flow (see the review of recent results in Zikanov *et al.* 2021), on the contrary, indicate that MCFs may disappear at high Ha , so the extrapolation can be wrong. The nature of the convection flow at the parameters corresponding to ducts in blankets and divertors of an operating fusion reactor remains unknown, setting up the motivation for the present study.

The focus of our investigation is on the magnetoconvection in the range of very high Gr and Ha including the values typical for a reactor blanket and divertor. To the best of our knowledge, this study is the first to analyze the MCF effect in this range. Linear stability analysis and DNS of flows in a horizontal duct with $Pr = 0.025$, $Re = 5000$, $10^8 \leq Gr \leq 10^{10}$ and $10^3 \leq Ha \leq 10^4$ are performed. The study follows the work of Zhang & Zikanov (2014) but differs by much larger values of Gr and Ha and the aspect ratio $\Gamma = 3.5$ selected to match the new experimental facility (see, e.g., Belyaev *et al.* 2017), on which the same configuration is to be explored at $Ha \lesssim 10^3$ and $Gr \lesssim 10^8$ in the near future. Another essential difference between our work and the work by Zhang

& Zikanov (2014) is that we carry out an in-depth analysis of the accuracy of the two-dimensional approximation applied to Q2D flows at such high Ha .

2. Presentation of the problem

The flow of an incompressible, Newtonian, viscous, electrically conducting fluid (a liquid metal) with constant physical properties is considered. The fluid moves through a horizontal duct of aspect ratio $\Gamma = 3.5$ (see figure 1). Spatially uniform and time-independent magnetic field $\mathbf{B} = B\mathbf{e}_y$ is imposed in the horizontal transverse direction. All walls are perfectly electrically insulated. The top and side walls are perfectly thermally insulated. The bottom wall is subject to uniform heating with the heat flux of constant rate q . The no-slip boundary conditions for velocity are applied at the walls.

2.1. Physical model

The Boussinesq and quasi-static approximations are applied. The quasi-static approximation is valid at small Reynolds and Prandtl numbers and usually utilized in numerical, experimental and theoretical studies of MHD flows of liquid metals (Davidson 2016). The approximation implies that the imposed magnetic field \mathbf{B} is much stronger than the perturbations of the magnetic field \mathbf{b} induced by the electric currents caused by the fluid motion. The induced magnetic field can be neglected in the expressions of the Lorentz force and Ohm's law. Furthermore, the induced field is assumed to adjust instantaneously to changes of velocity field.

The governing equations are rendered non-dimensional using the duct half-width in the magnetic field direction d as the length scale, mean streamwise velocity U as the velocity scale, wall heating-based group qd/κ as the temperature scale, B as the scale of the magnetic field strength, and dUB as the scale of electric potential. The equations can be written as:

$$\frac{\partial \mathbf{u}}{\partial t} + (\mathbf{u} \cdot \nabla) \mathbf{u} = -\nabla p - \nabla \hat{p} - \nabla \tilde{p} + \frac{1}{Re} \nabla^2 \mathbf{u} + \mathbf{F}_b + \mathbf{F}_L, \quad (2.1)$$

$$\nabla \cdot \mathbf{u} = 0, \quad (2.2)$$

$$\frac{\partial \theta}{\partial t} + \mathbf{u} \cdot \nabla \theta = \frac{1}{RePr} \nabla^2 \theta - u_x \frac{dT_m}{dx}, \quad (2.3)$$

where \mathbf{u} is the velocity field. The decompositions of the temperature and pressure fields commonly used in studies of mixed convection in ducts and pipes (see, e.g., Alboussi ere *et al.* 1993; Lyubimova *et al.* 2009; Zikanov *et al.* 2013; Zhang & Zikanov 2014; Zikanov *et al.* 2021) are applied. The decompositions are convenient, since they allow one to recast the problem in terms of the fluctuation fields, which are statistically uniform in the streamwise direction and, thus, study the flow in a relatively short segment of the channel with periodic inlet-exit conditions. The temperature field is written as a sum

$$T(\mathbf{x}, t) = T_m(x) + \theta(\mathbf{x}, t) \quad (2.4)$$

of fluctuations θ and the mean-mixed temperature $T_m(x) = A^{-1} \int_A u_x T dA$, where A is the cross-section area of the duct. One can also use the decomposition into fluctuations and simple mean temperature $\bar{T}(x) = A^{-1} \int_A T dA$. Applying the energy balance between the wall heating and the streamwise convection heat transfer, we find that $T_m(x)$ and $\bar{T}(x)$ are linear functions with the same derivative:

$$\frac{dT_m}{dx} = \frac{d\bar{T}}{dx} = \frac{\Pi}{APe} = \frac{\Gamma}{2Pe}, \quad (2.5)$$

where Π is the perimeter of the heated portion of the wall.

The total pressure P is presented in (2.1) as

$$P = \hat{p}(x) + \tilde{p}(x, z) + p(\mathbf{x}, t), \quad (2.6)$$

where $p(\mathbf{x}, t)$ is the field of pressure fluctuations statistically homogeneous in the streamwise direction, and \hat{p} is a linear function of x corresponding to the spatially uniform streamwise gradient $d\hat{p}/dx$ applied as a flow-driving mechanism. In the simulations discussed in this paper, the gradient is adjusted at every time step to maintain constant mean velocity.

The third term of the decomposition becomes necessary in numerical models of mixed convection in non-vertical channels with periodic inlet–exit conditions. The component

$$\tilde{p}(x, z) = \frac{dT_m}{dx} \frac{Gr}{Re^2} xz = \frac{\Pi}{ARePr} \frac{Gr}{Re^2} xz, \quad (2.7)$$

arises due to the buoyancy force caused by the mean–mixed temperature T_m :

$$\mathbf{F}_{b,m} = GrRe^{-2} \mathbf{e}_z T_m, \quad (2.8)$$

where \mathbf{e}_z is the unit vector opposite to the direction of gravity (see figure 1). The force has a non-zero curl and, therefore, modifies the velocity field. Its action on the flow can be described by introducing the pressure field \tilde{p} , such that its vertical gradient balances $\mathbf{F}_{b,m}$. The pressure field is a two-dimensional function increasing with the streamwise coordinate x and vertical coordinate z . Its z -dependent x -gradient, which appears in the respective momentum equation, generates a flow in the positive x -direction in the lower part of the channel and in the negative x -direction in the upper part. The result is a top–bottom asymmetry of the streamwise velocity profile and of the associated convection heat flux, which can dramatically change the structure of the flow at high Gr and Ha (see Zikanov *et al.* 2013; Zhang & Zikanov 2014, 2017; Zikanov *et al.* 2021).

The buoyancy force in (2.1) is

$$\mathbf{F}_b = GrRe^{-2} \mathbf{e}_z T. \quad (2.9)$$

The Lorentz force is computed as

$$\mathbf{F}_L = Ha^2 Re^{-1} \mathbf{j} \times \mathbf{e}_y, \quad (2.10)$$

where \mathbf{e}_y is the unit vector along the imposed magnetic field (see figure 1). The electric current \mathbf{j} is determined by the Ohm’s law

$$\mathbf{j} = -\nabla\phi + (\mathbf{u} \times \mathbf{e}_y), \quad (2.11)$$

where the electric potential ϕ is a solution of the Poisson equation expressing the instantaneous electric neutrality of the fluid:

$$\nabla^2\phi = \nabla \cdot (\mathbf{u} \times \mathbf{e}_y). \quad (2.12)$$

The inlet–exit conditions are those of periodicity of the velocity \mathbf{u} , temperature fluctuations θ , pressure fluctuations p , and potential ϕ .

2.2. Two-dimensional approximation

Flows with a very strong imposed magnetic field are considered, so the Hartmann number and the Stuart number satisfy $Ha \gg 1$ and $N \equiv Ha^2/Re \gg 1$, respectively. The flows are anticipated to have Q2D form with nearly zero gradients along the magnetic field lines except in the thin Hartmann layers at the walls perpendicular to the field. The 2D approximation proposed by Sommeria & Moreau (1982) can be applied in this asymptotic limit. The problem can be expressed in terms of the variables integrated wall-to-wall along the direction of the magnetic field, leading to 2D dynamics for y -averaged

quantities. The approximation has been verified and examined by Poth erat *et al.* (2000, 2005), and utilized in numerical studies of liquid metal flows in rectangular ducts (see, e.g., Poth erat 2007; Smolentsev *et al.* 2012; Vetcha *et al.* 2013; Vo *et al.* 2017; Zhang & Zikanov 2018).

The often applied abbreviation SM82 will be used for the model in the following. The y -independent solutions obtained in the framework of the model will be referred to as 2D solutions, while the full solutions obtained numerically without resorting to the model will be designated as 3D.

The SM82 model is derived for flows with $Ha \gg 1$ and $N \gg 1$, in domains with electrically insulating walls and constant wall-to-wall distance in the field direction. It utilizes the fact that the Lorentz force becomes nearly zero in Q2D flows in such geometries, and the effect of the magnetic field on the flow is largely reduced to the viscous friction in the thin Hartmann layers, which can be accurately modeled by the linear friction term in the momentum equation. In non-isothermal flows, the model can be extended to 2D approximation of temperature if the imposed heat flux is perpendicular to the magnetic field (see, e.g., Gelfgat & Molokov 2011; Vetcha *et al.* 2013; Zhang & Zikanov 2018).

The SM82 version of (2.1)–(2.3) is

$$\frac{\partial \mathbf{u}}{\partial t} + (\mathbf{u} \cdot \nabla) \mathbf{u} = -\nabla p - \nabla \hat{p} - \nabla \tilde{p} + \frac{1}{Re} \nabla^2 \mathbf{u} - \frac{Ha}{Re} \mathbf{u} + \frac{Gr}{Re^2} T \hat{e}_z, \quad (2.13)$$

$$\nabla \cdot \mathbf{u} = 0, \quad (2.14)$$

$$\frac{\partial \theta}{\partial t} + \mathbf{u} \cdot \nabla \theta = \frac{1}{RePr} \nabla^2 \theta - u_x \frac{dT_m}{dx}, \quad (2.15)$$

where all the flow variables are now 2D fields obtained by wall-to-wall averaging. The term $(Ha/Re)\mathbf{u}$ represents the effect of friction in the Hartmann layers.

2.3. Numerical method

The governing equations (2.1)–(2.3) and (2.13)–(2.15) are solved numerically using the finite difference scheme introduced by Krasnov *et al.* (2011), and later developed, tested and applied to high- Ha flows and flows with thermal convection in numerous works including those by Krasnov *et al.* (2012), Zhao & Zikanov (2012), Zikanov *et al.* (2013), Zhang & Zikanov (2014), and Gelfgat & Zikanov (2018). The spatial discretization is of the second order and nearly fully conservative with regards to the mass, momentum, electric charge, kinetic energy and thermal energy conservation principles (Ni *et al.* 2007; Krasnov *et al.* 2011). The computational grid is clustered towards the walls according to the coordinate transformation in the horizontal direction $y = \tanh(A_y \eta) / \tanh(A_y)$ and in the vertical direction $z = \tanh(A_z \xi) / \tanh(A_z)$. Here η and ξ are the transformed coordinates, in which the grid is uniform, and A_y and A_z are the coefficients determining the degrees of clustering. The time discretization is implicit for the conduction and viscosity terms and based on the Adams–Bashforth/backward-differentiation method of the second order and the standard projection algorithm (see, e.g., Zikanov 2019). The nonlinear convection and body force terms are treated explicitly. The elliptic equations for potential, pressure, temperature and velocity components are solved using the Fourier decomposition in the streamwise coordinate and the direct cyclic reduction solution of the 2D equations for Fourier components conducted on the transformed grid (see Krasnov *et al.* 2011).

The algorithm is parallelized using the hybrid MPI-OpenMP approach. The MPI memory distribution is along the y -coordinate in the physical space and along the streamwise wavenumber in the Fourier space.

2.4. Approach to linear stability analysis

The base flow needs to be selected before conducting the linear stability analysis. We note that an archetypal structure of a laminar flow with convection in a horizontal channel heated from below is a superposition of the streamwise flow $u_x(y, z)$ and one or several streamwise-uniform convection rolls $(u_y(y, z), u_z(y, z))$. At high Ha , the structure can be modified by the magnetic field and replaced by a 3D structure with the rolls aligned with the magnetic field and, thus, x -dependent velocity and temperature at high Ha . Following Zikanov *et al.* (2013) and Zhang & Zikanov (2014), we treat the problem as that of the instability of the laminar steady-state streamwise-uniform base flow $\mathbf{U}(y, z)$, $\Theta(y, z)$, $P(y, z)$ to x -dependent perturbations.

The base flow is calculated by artificially imposing uniformity in the streamwise direction, i.e. by applying x -averaging after every time step. In order to assure that a fully developed state of the base flow is reached, each solution is computed for sufficiently long time. Long evolution, in some regimes up to 1000 time units, is typically required in order to arrive at this state. No unsteady base flow solutions have been detected in the studied range of parameters. The steady-state solutions are discussed in section 3.1.

The linear stability analysis is conducted using a modified version of the numerical model described in section 2.3. We follow evolution of perturbations - solutions of the equations linearized around the base flow $\mathbf{U}(y, z)$, $\Theta(y, z)$, $P(y, z)$. The evolution of individual Fourier modes determined by their streamwise wavelengths λ is computed.

The linear instability is identified by the exponential growth of the perturbations with the growth rate determined as

$$\gamma = \frac{1}{2E'} \frac{dE'}{dt}, \quad (2.16)$$

where $E' = \langle f^2 \rangle$, $\langle \dots \rangle$ stands for volume averaging, and f stands for perturbations of a velocity component or temperature. The growth rate coefficient is recorded after its values computed for all three velocity components and temperature coincide with each other and remain constant within the third digit after the decimal point for at least 100 time units. The results of the linear stability analysis are presented in sections 3.3 and 3.4.

2.5. Grid sensitivity study

The grid sensitivity study has been conducted for the base flow. A detailed description of the various flow regimes is provided in section 3.1. For the present discussion, it is sufficient to say that accurate resolution of the internal flow structure, along with two boundary layers: the Hartmann layers of thickness $\delta_{Ha} \sim Ha^{-1}$ at the vertical walls and the Shercliff layers of thickness $\delta_{Sh} \sim Ha^{-1/2}$ at the top and bottom walls, is critically important for accurate representation of the flow behavior.

As an example, the results obtained at $Ha = 1200$, $Gr = 10^8$ are presented in table 1. In a fully developed steady-state flow, the integrated Lorentz and buoyancy forces are zero. The wall friction must be balanced by the driving pressure gradient according to

$$\frac{d\hat{p}}{dx} = A^{-1} (\tau_{Ha} + \tau_{Sh}), \quad (2.17)$$

where τ_{Ha} and τ_{Sh} are the computed values of the integrated friction forces at the Hartmann and Shercliff walls of the duct, respectively, expressed as

$$\tau_{Ha} = \tau_y = \frac{1}{Re} \sum_{y=\pm 1} \int_{-2/\Gamma}^{2/\Gamma} \frac{\partial U_x}{\partial y} dz, \quad \tau_{Sh} = \tau_z = \frac{1}{Re} \sum_{z=\pm 2/\Gamma} \int_{-1}^1 \frac{\partial U_x}{\partial z} dy. \quad (2.18)$$

Values of τ_{Ha} , τ_{Sh} and the error ϵ , with which the computed solution satisfies (2.17),

N_y	N_z	A_y	A_z	$-\tau_{Ha}$	$-\tau_{Sh}$	ϵ	N_{Ha}	N_{Sh}
128	32	4.0	2.0	0.23425	0.02914	0.00074	6	10
128	64	4.0	2.0	0.23460	0.26417	0.00070	6	21
128	64	4.3	2.0	0.23477	0.26387	0.00025	8	21
128	96	4.0	2.0	0.23468	0.26407	0.00069	6	32
128	96	4.3	2.0	0.23484	0.26377	0.00024	8	32
192	96	4.0	2.0	0.23459	0.26356	0.00030	9	32
192	128	4.0	2.0	0.23462	0.26347	0.00029	9	43

TABLE 1. Grid sensitivity study conducted for $Ha = 1200$ and $Gr = 10^8$: τ_{Ha} and τ_{Sh} are the wall friction forces, ϵ is the absolute error of the balance (2.17). The number of grid points inside the Hartmann and Shercliff boundary layers are N_{Ha} and N_{Sh} , respectively.

found on various grids are compared in table 1. On the basis of these data, we conclude that the grid with $N_y \times N_z = 192 \times 96$, $A_y = 4.0$ and $A_z = 2.0$ is sufficient. The maximum and minimum grid steps of such a grid are $\Delta y_{min} \approx 0.0001$, $\Delta y_{max} \approx 0.042$, $\Delta z_{min} \approx 0.0009$, $\Delta z_{max} \approx 0.012$. The Hartmann and Shercliff layers are resolved by, respectively, 9 and 32 grid points.

The parameters of the grids in the entire studied parameter range of Ha and Gr have been determined in the same way. It has been found that the value of Gr does not affect the selection at fixed Ha . This effect can be explained by the presence of very strong magnetic fields which fully suppress transverse circulation (see section 3.1 for a discussion). The summary of the grids used in the simulations is presented in table 2.

A grid sensitivity study has also been conducted to determine the minimum number of grid points N_x required in the linear stability analysis. It has been found that the growth of linear unstable modes is accurately reproduced at $N_x = 32$ for modes with $\lambda \lesssim 2$, which needs to be increased to $N_x = 64$ for greater λ .

Computational domains of length $L_x = 4\pi$ or $L_x = 2\pi$ are used in DNS. As we will see below, these lengths are substantially larger than the streamwise wavelength of the fastest growing instability modes. The flow structures have been accurately resolved with, respectively, 384 or 192 grid points in the x -direction.

The time steps adjusted to secure numerical instability and, thus, varying with Ha and Gr , but never exceeding 2.5×10^{-3} , are used in linear stability and DNS simulations.

3. Results

3.1. Base flow

The flow structure for several typical cases is illustrated in figures 2 and 3. The results for all the completed simulations are summarized in table 3. The table shows the type of the flow for a particular regime (Q2D or 3D flows to be discussed shortly), the maximum and minimum values of U_x , integral quantities, such the wall friction force $d\hat{p}/dx$, the volume-averaged kinetic energies of streamwise and transverse velocities

$$E_x = A^{-1} \int_{-1}^1 \int_{-1}^1 U_x^2 dydz, \quad E_t = A^{-1} \int_{-1}^1 \int_{-1}^1 (U_y^2 + U_z^2) dydz, \quad (3.1)$$

and the mean square of temperature perturbations

$$E_\theta = A^{-1} \int_{-1}^1 \int_{-1}^1 \Theta^2 dydz. \quad (3.2)$$

Ha	N_y	N_z	A_y	A_z	N_{Ha}	N_{Sh}
1000	192	96	4.0	2.0	9	32
2000	256	96	4.0	2.0	8	28
3000	384	96	4.0	2.0	9	24
4000	384	96	4.0	2.0	7	22
5000	512	96	4.0	2.0	8	20
6000	512	96	4.0	2.0	7	19
7000	512	96	4.3	2.0	9	18
8000	512	96	4.3	2.0	8	17
9000	512	96	4.3	2.0	7	16
10000	512	96	4.3	2.0	6	15

TABLE 2. Parameters of the computational grids used in the simulations for $Gr = 10^8 - 10^{10}$. The number of grid points inside the Hartmann and Shercliff boundary layers are N_{Ha} and N_{Sh} , respectively.

Similar data for flows with lower values of Gr and Ha in a duct with $\Gamma = 1$ can be found in (Zhang & Zikanov 2014).

The flow structure is predominantly determined by the effect of magnetoconvection. Similarly to the findings of Zhang & Zikanov (2014), we observe two regimes of the base flow depending on whether Gr is smaller or larger than a certain threshold $Gr^*(Ha)$. The Q2D regime observed at $Gr < Gr^*$ is characterized by the transverse convection-induced circulation entirely suppressed by the strong magnetic field. The distributions of the temperature and streamwise velocity are nearly one-dimensional outside of the Hartmann boundary layers ($\Theta \approx \Theta(z)$ and $U_x \approx U_x(z)$). In the absence of transverse circulation, the distributions of temperature are determined by the balance between the heat conduction and the heat convection by U_x . Examples of this regime are shown in figure 2a and figure 3.

The 3D regime observed at $Gr > Gr^*(Ha)$, when the strength of the magnetic field is insufficient to suppress convection circulation, is characterized by significant transverse flow and fully 2D variations of temperature. (see figure 2b – e).

To avoid confusion, it is pertinent to repeat the terminology here. The terms 3D and Q2D are used in this paper to describe the general flow transformation caused by the magnetic field, i.e. suppression of velocity and temperature gradients along the magnetic field lines in the core of the duct and formation of thin Hartmann boundary layers. The base flow, in which streamwise uniformity is also imposed, becomes, respectively, 2D and Q1D.

We find the Q2D regime in the larger part of the explored range of Ha and Gr including the most interesting cases of large Ha (see the rightmost column in table 3). The total friction force increases at stronger magnetic fields. The visible effect of convection is the asymmetry of the velocity profile, with U_x larger in the bottom than in the top half (see, e.g., figure 3b, d). The cause of the asymmetry has been explained in section 2.1.

The 3D regimes are only found in a limited range of moderate values of Ha at $Gr = 10^9$ and 10^{10} (see table 3). The transverse circulation consist of a single roll (see figure 2b, e) or two symmetric rolls (see figure 2c, d). The single roll has no preferred circulation direction and may appear in the solution either as shown in the figure 2b or as a symmetric reflection with respect to the vertical midplane (see figure 2e for an example). The circulation causes a visibly 2D distributions of Θ and U_x , and, at the same values of Gr , a decrease of E_θ as a result of mixing (see table 3). We observe stronger top–bottom asymmetries or even formation of reverse flow in the top portion of the duct as the

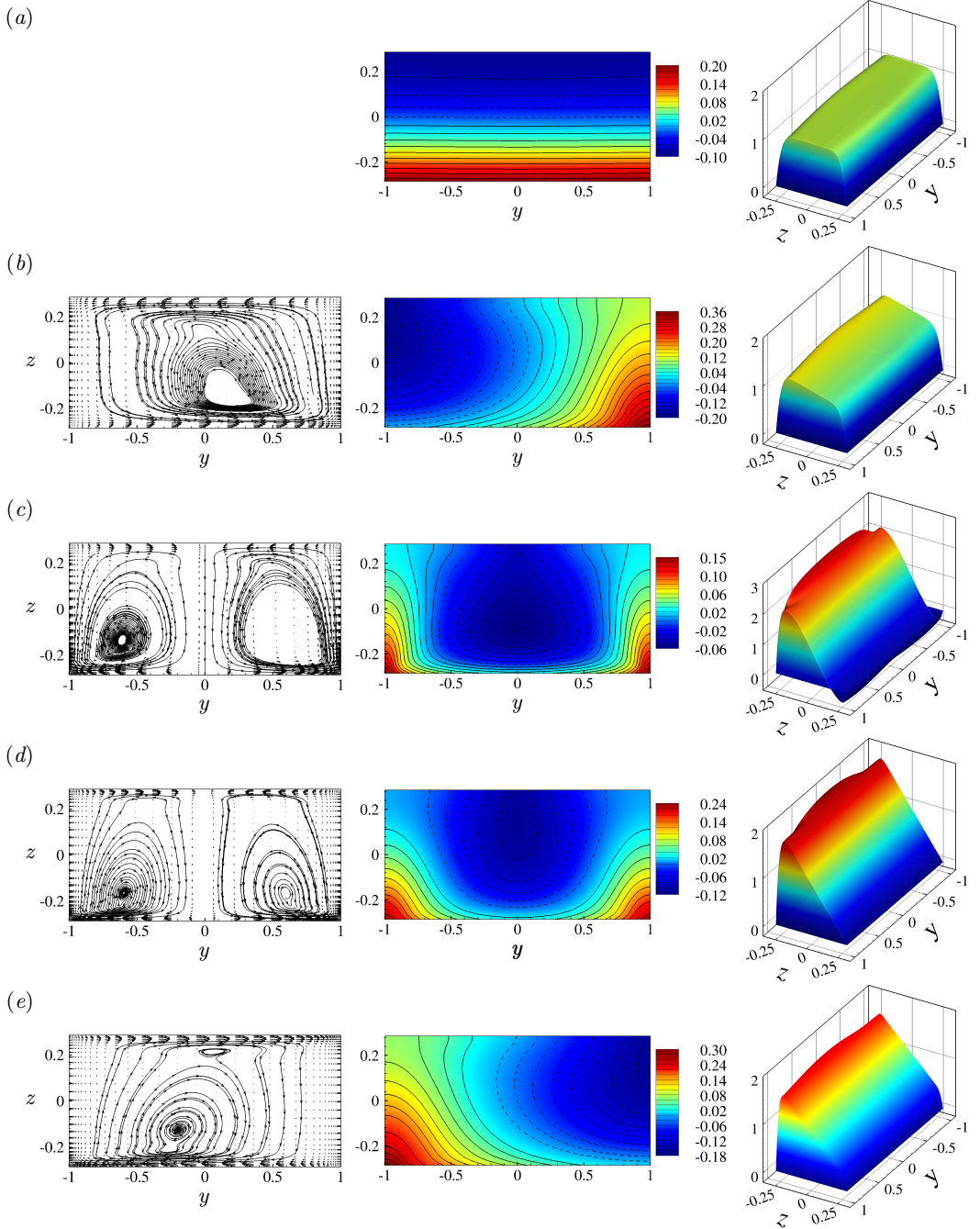


FIGURE 2. Base flow at $Ha = 1000$, $Gr = 10^8$ (a), $Ha = 1000$, $Gr = 10^9$ (b), $Ha = 1000$, $Gr = 10^{10}$ (c), $Ha = 2000$, $Gr = 10^{10}$ (d) and $Ha = 3000$, $Gr = 10^{10}$ (e). Vector fields and streamlines of transverse circulation (u_y , u_z) are shown in the left column (not in (a), since the velocity's amplitude is virtually zero in this case). The middle and right columns show distributions of temperature fluctuations and streamwise velocity u_x , respectively. Solid and dashed isolines in the middle column indicate positive and negative values, respectively. The wall heating is at $z = -0.2857$, and the magnetic field is in the y -direction.

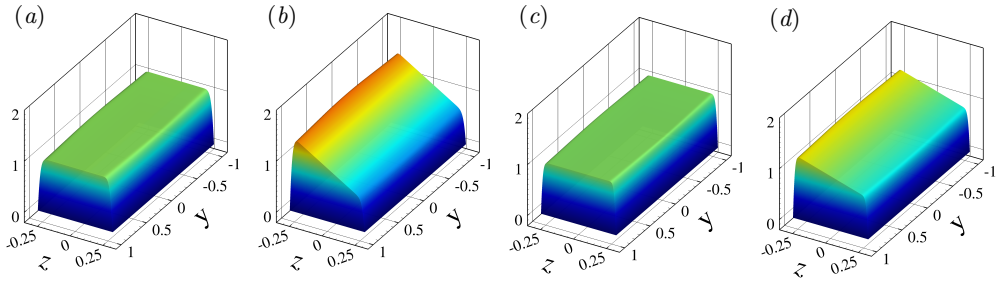


FIGURE 3. Q2D base flow at $Ha = 5000$, $Gr = 10^9$ (a), $Ha = 5000$, $Gr = 10^{10}$ (b), $Ha = 10000$, $Gr = 10^9$ (c) and $Ha = 10000$, $Gr = 10^{10}$ (d). Distribution of streamwise velocity u_x is shown. The wall heating is at $z = -0.2857$, and the magnetic field is in the y -direction.

Ha	Gr	Gr/Ha^2	$-\hat{d}p/dx$	E_x	E_t	E_θ	$u_{x,min}$	$u_{x,max}$	Regime
1000	10^8	1.00×10^2	0.222	1.050	1.62×10^{-8}	3.59×10^{-3}	0.0	1.139	Q2D
1000	10^9	1.00×10^3	0.224	1.056	6.32×10^{-3}	9.31×10^{-3}	0.0	1.249	3D
1000	10^{10}	1.00×10^4	0.254	1.892	3.11×10^{-2}	7.11×10^{-4}	-0.402	2.601	3D
2000	10^8	2.50×10^1	0.430	1.035	5.42×10^{-9}	3.61×10^{-3}	0.0	1.079	Q2D
2000	10^9	2.50×10^2	0.431	1.037	4.96×10^{-7}	3.34×10^{-3}	0.0	1.153	Q2D
2000	10^{10}	2.50×10^3	0.447	1.313	8.30×10^{-3}	2.19×10^{-3}	0.0	1.968	3D
3000	10^8	1.11×10^1	0.636	1.029	1.76×10^{-9}	3.62×10^{-3}	0.0	1.063	Q2D
3000	10^9	1.11×10^2	0.637	1.030	1.66×10^{-7}	3.45×10^{-3}	0.0	1.114	Q2D
3000	10^{10}	1.11×10^3	0.643	1.172	1.58×10^{-2}	4.48×10^{-3}	0.0	1.683	3D
4000	10^8	6.25×10^0	0.842	1.025	3.85×10^{-10}	3.63×10^{-3}	0.0	1.054	Q2D
4000	10^9	6.25×10^1	0.842	1.026	3.70×10^{-8}	3.53×10^{-3}	0.0	1.093	Q2D
4000	10^{10}	6.25×10^2	0.847	1.109	2.75×10^{-6}	2.96×10^{-3}	0.0	1.522	Q2D
5000	10^8	4.00×10^0	1.046	1.022	1.13×10^{-10}	3.63×10^{-3}	0.0	1.048	Q2D
5000	10^9	4.00×10^1	1.046	1.023	1.10×10^{-8}	3.57×10^{-3}	0.0	1.080	Q2D
5000	10^{10}	4.00×10^2	1.049	1.078	8.55×10^{-7}	3.16×10^{-3}	0.0	1.425	Q2D
6000	10^8	2.78×10^0	1.251	1.020	1.00×10^{-10}	3.63×10^{-3}	0.0	1.043	Q2D
6000	10^9	2.78×10^1	1.251	1.021	9.79×10^{-9}	3.57×10^{-3}	0.0	1.071	Q2D
6000	10^{10}	2.78×10^2	1.254	1.060	7.75×10^{-7}	3.18×10^{-3}	0.0	1.362	Q2D
7000	10^8	2.04×10^0	1.454	1.019	9.00×10^{-11}	3.63×10^{-3}	0.0	1.040	Q2D
7000	10^9	2.04×10^1	1.454	1.019	8.80×10^{-9}	3.58×10^{-3}	0.0	1.064	Q2D
7000	10^{10}	2.04×10^2	1.457	1.048	7.12×10^{-7}	3.20×10^{-3}	0.0	1.315	Q2D
8000	10^8	1.56×10^0	1.658	1.018	8.12×10^{-11}	3.63×10^{-3}	0.0	1.037	Q2D
8000	10^9	1.56×10^1	1.658	1.018	7.96×10^{-9}	3.58×10^{-3}	0.0	1.058	Q2D
8000	10^{10}	1.56×10^2	1.661	1.040	6.56×10^{-7}	3.22×10^{-3}	0.0	1.280	Q2D
9000	10^8	1.23×10^0	1.862	1.017	2.50×10^{-11}	3.63×10^{-3}	0.0	1.035	Q2D
9000	10^9	1.23×10^1	1.862	1.017	2.46×10^{-9}	3.60×10^{-3}	0.0	1.054	Q2D
9000	10^{10}	1.23×10^2	1.864	1.035	2.11×10^{-7}	3.34×10^{-3}	0.0	1.252	Q2D
10000	10^8	1.00×10^0	2.067	1.016	2.31×10^{-11}	3.63×10^{-3}	0.0	1.033	Q2D
10000	10^9	1.00×10^1	2.067	1.016	2.28×10^{-9}	3.60×10^{-3}	0.0	1.050	Q2D
10000	10^{10}	1.00×10^2	2.068	1.031	1.97×10^{-7}	3.36×10^{-3}	0.0	1.229	Q2D

TABLE 3. Integral characteristics and type of the computed base flow states.

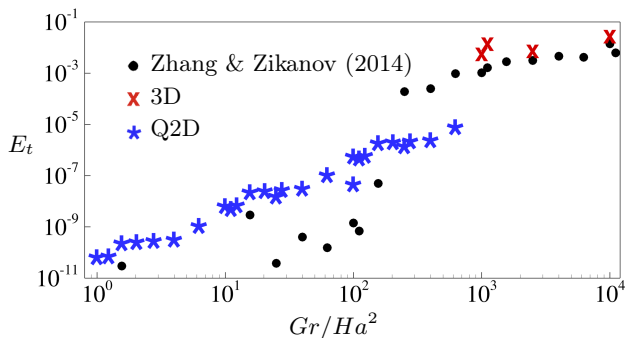


FIGURE 4. The average kinetic energy of transverse circulation in the base flow E_t as a function of Gr/Ha^2 . Circles indicate the numerical results of Zhang & Zikanov (2014) at $\Gamma = 1.0$. Stars and crosses indicate, respectively, Q2D and 3D regimes found in this work for the flow at $\Gamma = 3.5$. Values of E_t and Gr/Ha^2 for each computed flow can be found in table 3.

strength of convection increases at fixed Ha (see figure 2a – c for an example). As an illustration of the asymmetry the minimum and maximum values of u_x are shown in table 3.

The classification of the flow regimes into Q2D and 3D can also be described in terms of the values of the average kinetic energy of transverse circulation E_t . Our data shown in table 3 and figure 4 are in a good qualitative agreement with the results of Zhang & Zikanov (2014). The observed differences can be attributed to the substantially different studied ranges of Ha and Gr and different aspect ratio.

We see in figure 4 that, at a fixed Reynolds number considered in this work, the intensity of the transverse circulation is well approximated by a function of the single control parameter - the combination Gr/Ha^2 . Analyzing the flow structures at various values of E_t we find a clear demarcation between 3D and Q2D regimes. E_t is greater than, approximately, 10^{-4} in 3D regimes. Q2D flows all have values of E_t less than 10^{-6} .

Our interest in this study is primarily in the Q2D regimes. The 3D regimes are not considered in the rest of the paper.

3.2. Applicability of the SM82 model

In this section, we investigate the applicability of the SM82 model to analysis of magnetoconvection instability.

3.2.1. Base flow

For a streamwise-uniform, unidirectional, steady-state base flow, the SM82 model equations (2.13)–(2.15) are reduced to a system of linear ordinary differential equations. The solution satisfying the boundary conditions is:

$$U_x(z) = C \frac{Re}{Ha} c_1 + A \frac{Re}{Ha\Gamma} s_1 - A \frac{Re}{Ha} z - C \frac{Re}{Ha}, \quad (3.3)$$

$$\Theta(z) = \frac{C}{2} \frac{Re\Gamma}{Ha^2} c_1 + \frac{A}{2} \frac{Re}{Ha^2} s_1 - \frac{A}{12} \frac{Re\Gamma}{Ha} z^3 - \frac{C}{4} \frac{Re\Gamma}{Ha} z^2 + a_1 z, \quad (3.4)$$

where

$$a_1 = -\frac{C}{2} \frac{Re\Gamma}{Ha^{3/2}} t_1 - \frac{A}{2} \frac{Re\Gamma}{Ha^{3/2}} t_1^{-1} + \frac{A}{4} \frac{Re}{Ha\Gamma} + \frac{C}{2} \frac{Re}{Ha}, \quad (3.5)$$

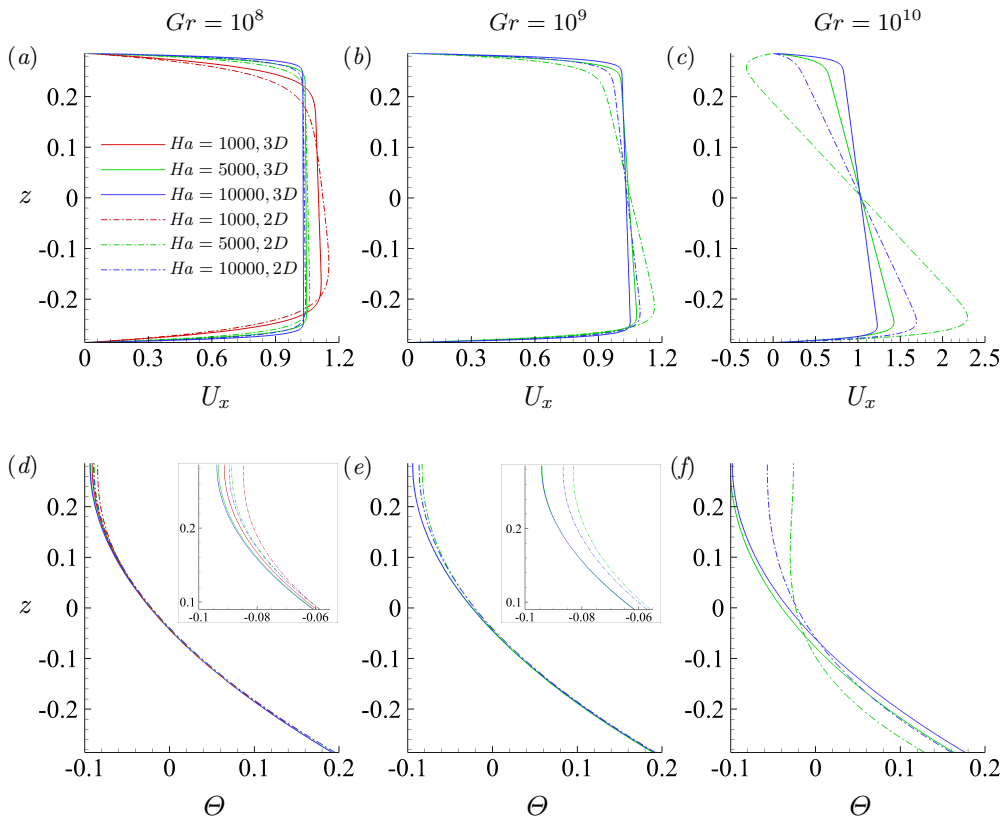


FIGURE 5. Base flow profiles at $Gr = 10^8$ (a, d), $Gr = 10^9$ (b, e), and $Gr = 10^{10}$ (c, f). The SM82 model solutions (3.3), (3.4) and the distributions along the midplane $y = 0$ obtained in the full numerical solutions of section 3.1 are denoted, respectively, as 2D and 3D. The curves for $Ha = 10^3$ are only shown at $Gr = 10^8$ (a, d), since at higher Gr the base flow is not Q2D (see section 3.1). The top and bottom rows show the profiles of streamwise velocity and temperature, respectively. The insets in (d) and (e) show zoomed-in illustrations of the temperature profiles near the top wall.

$$c_1 = \frac{\cosh(\sqrt{Ha}z)}{\cosh(\sqrt{Ha}/\Gamma)}, \quad s_1 = \frac{\sinh(\sqrt{Ha}z)}{\sinh(\sqrt{Ha}/\Gamma)}, \quad t_1 = \tanh(\sqrt{Ha}/\Gamma), \quad (3.6)$$

$$A = \frac{\Gamma}{2RePr} \frac{Gr}{Re^2}, \quad C = \frac{Ha}{Re\Gamma} \frac{1}{t_1/\sqrt{Ha} - 1/\Gamma}. \quad (3.7)$$

The profiles (3.3) and (3.4) are shown for $Gr = 10^8, 10^9, 10^{10}$ and several values of Ha in figure 5. For comparison, respective profiles of the true U_x and Θ obtained for the computed base flow solutions described in section 3.1 are shown for the midplane $y = 0$. The symbols 2D and 3D correspond to, respectively, approximate SM82 and computed solutions.

Good agreement between the computed solutions and the solutions of the SM82 model is evident at $Gr = 10^8$ and 10^9 . There are some deviations between the computed and model profiles of U_x , but they are small and decrease with increasing Ha . The agreement is significantly worse in the case of the flows at $Gr = 10^{10}$. Here we observe large deviations between the computed and model curves at $Ha = 5000$ and smaller, yet still significant deviations at $Ha = 10000$.

Ha	Gr	λ										
		0.2	0.3	0.4	0.5	0.6	0.7	0.8	0.9	1.0	1.5	2.0
1000	10^8	–	0.164	0.360	0.474	0.532	0.553	0.552	0.538	0.518	0.396	0.301
<u>1000</u>	<u>10^8</u>	–	<u>0.049</u>	<u>0.269</u>	<u>0.398</u>	<u>0.461</u>	<u>0.486</u>	<u>0.487</u>	<u>0.475</u>	<u>0.455</u>	<u>0.338</u>	<u>0.247</u>
2000	10^8	–	–	0.251	0.387	0.461	0.495	0.504	0.499	0.485	0.381	0.295
<u>2000</u>	<u>10^8</u>	–	–	<u>0.200</u>	<u>0.345</u>	<u>0.486</u>	<u>0.422</u>	<u>0.456</u>	<u>0.459</u>	<u>0.445</u>	<u>0.344</u>	<u>0.261</u>
2000	10^9	1.563	2.602	3.010	3.136	3.134	3.069	2.972	2.859	2.741	2.175	–
<u>2000</u>	<u>10^9</u>	<u>1.028</u>	<u>2.029</u>	<u>2.459</u>	<u>2.626</u>	<u>2.671</u>	<u>2.651</u>	<u>2.593</u>	<u>2.513</u>	<u>2.421</u>	<u>1.941</u>	–
3000	10^9	1.540	2.587	2.993	3.117	3.114	3.048	2.950	2.836	2.715	2.141	–
<u>3000</u>	<u>10^9</u>	<u>1.085</u>	<u>2.162</u>	<u>2.619</u>	<u>2.791</u>	<u>2.827</u>	<u>2.792</u>	<u>2.717</u>	<u>2.622</u>	<u>2.516</u>	<u>1.990</u>	–
4000	10^{10}	10.234	11.553	11.674	11.435	11.067	10.645	10.202	9.754	9.312	–	–
<u>4000</u>	<u>10^{10}</u>	<u>6.881</u>	<u>7.404</u>	<u>7.415</u>	<u>7.156</u>	<u>6.833</u>	<u>6.494</u>	<u>6.158</u>	<u>5.834</u>	<u>5.525</u>	–	–
5000	10^{10}	10.605	11.918	12.023	11.764	11.371	10.925	10.458	9.988	9.527	–	–
<u>5000</u>	<u>10^{10}</u>	<u>7.454</u>	<u>8.269</u>	<u>8.273</u>	<u>8.018</u>	<u>7.673</u>	<u>7.303</u>	<u>6.934</u>	<u>6.577</u>	<u>6.237</u>	–	–
10000	10^{10}	10.807	12.064	12.106	11.791	11.351	10.865	10.366	9.871	9.389	–	–
<u>10000</u>	<u>10^{10}</u>	<u>8.729</u>	<u>9.890</u>	<u>9.942</u>	<u>9.668</u>	<u>9.291</u>	<u>8.882</u>	<u>8.468</u>	<u>8.059</u>	<u>7.661</u>	–	–

TABLE 4. Results of the linear stability analysis of 3D and 2D flow solutions. Rates of exponential growth γ are shown as functions of the axial wavelength λ . The results of the SM82 model are underlined. The growth rates are determined as in (2.16).

3.2.2. Linear stability analysis

In order to verify applicability of the SM82 model to linear stability analysis of Q2D flows, instability of several high- Ha flows was evaluated twice: once using full 3D model of the base flow and perturbations and once entirely in the framework of the 2D SM82 model. The results are presented in figure 6 and table 4. We see good agreement between predictions of 2D and 3D models at $Gr = 10^8$ and 10^9 . The accuracy improves with growing Ha . As an example, the average relative difference between the values of the growth rate γ for the two models is 33% at $Ha = 2000$, $Gr = 10^9$ and 11% at $Ha = 3000$, $Gr = 10^9$. The situation is less clear for flows at $Gr = 10^{10}$ (see figure 6c and the last six lines of table 4). Here we only see a qualitative agreement. The shape of the $\gamma(\lambda)$ curves, the wavelength of the most unstable mode, and the effect of Ha on stability are similar in the 3D and 2D solution. The quantitative agreement is, however, poor, with the difference between the values of γ found for the two models being about 50%.

The quantitative disagreement between the base flow profiles and, as an evident consequence, stability properties found in the 3D and 2D models is difficult to interpret. The velocity and temperature distributions computed in the framework of the 3D model clearly show that the base flow is Q2D and nearly perfectly unidirectional at Ha higher than approximately 4000 (see figure 3b, d and values of E_t in table 3). As illustrated in section 3.3, fields of growing perturbations also remain Q2D at such high Ha . Additional calculations performed with larger grids and longer times of flow evolution did not lead to significant changes. The deviations from quasi-two-dimensionality and inaccuracy of the numerical model are, therefore, excluded as possible reasons.

A further useful, albeit not fully explaining illustration is provided in figure 7. Computed base flow distributions of U_x and the streamwise component of the Lorentz force F_{Lx} are shown for $Ha = 10000$ and $Gr = 10^8, 10^9$ and 10^{10} within and near the Hartmann boundary layer. We see that the strong vertical variation of U_x existing at $Gr = 10^{10}$ extends toward the Hartmann wall and causes a respective variation of the Lorentz force. It must be noted that this picture does not contradict to the identification of the flow

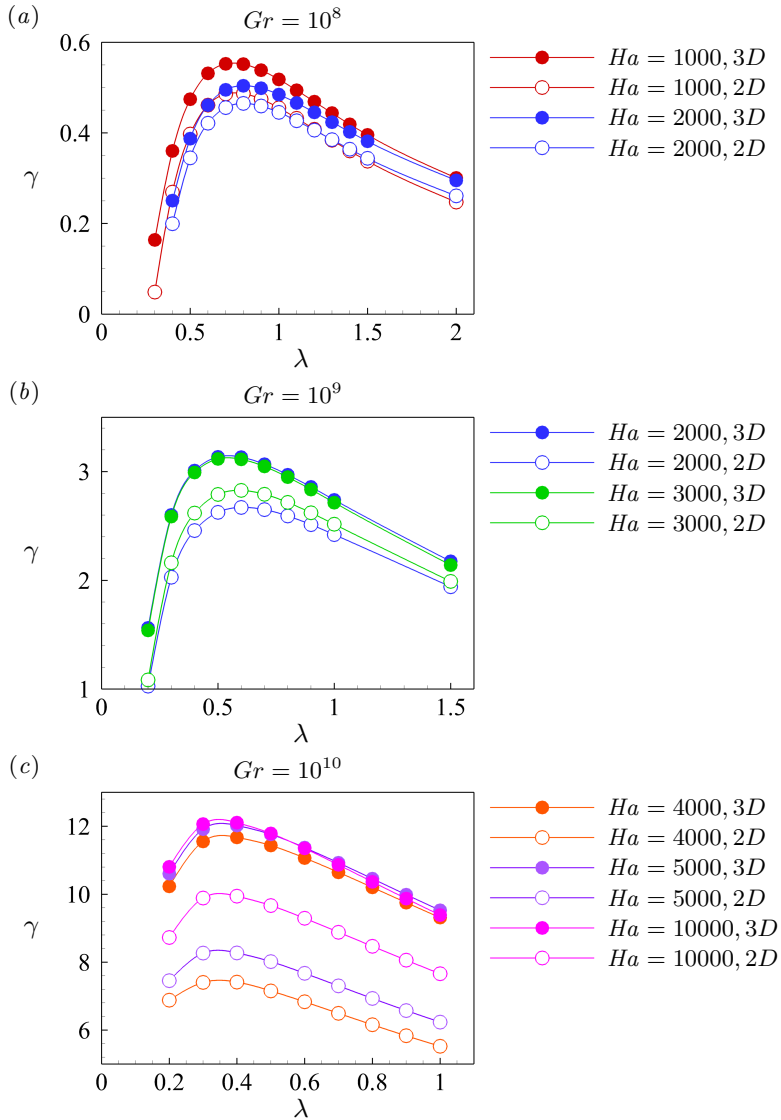


FIGURE 6. Rates of exponential growth γ shown as functions of the axial wavelength λ at $Ha = 1000, 2000$, $Gr = 10^8$ (a), $Ha = 2000, 3000$, $Gr = 10^9$ (b), and $Ha = 4000, 5000$, $Gr = 10^{10}$ (c). The results of 3D and 2D (SM82) models are denoted as filled and empty circles, respectively.

as Q2D. The profiles $U_x(y, z = const)$ collapse into one curve corresponding to the Hartmann profile if taken outside the sidewall layers at the horizontal walls and scaled by the respective maximum values of U_x .

3.2.3. Nonlinear flows

The results presented so far in this section indicate that the SM82 2D model may also inaccurately describe the nonlinear flow regimes developing as a result of the instability at $Gr = 10^{10}$. As a test of this possibility, comparison between the results of 2D and 3D models at $Gr = 10^{10}$, $Ha = 10000$ is illustrated in figures 8 and 9 and discussed below. The procedure of computing nonlinear flows is described in section 3.4. Here we only mention that the same numerical resolution is used in 2D and 3D models. The shorter

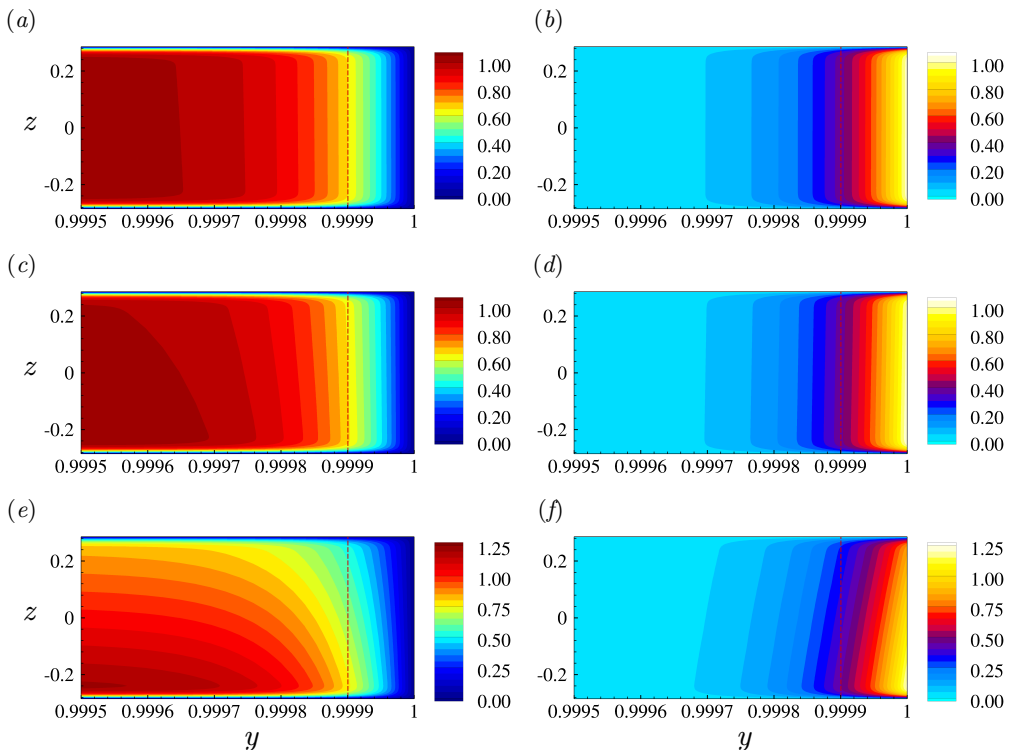


FIGURE 7. Base flow at $Gr = 10^8$ (a, b), $Gr = 10^9$ (c, d), and $Gr = 10^{10}$ (e, f) for $Ha = 10000$. The left and right columns show, respectively, distributions of streamwise velocity U_x and the streamwise component of the Lorentz force F_{Lx} near the Hartmann wall. The red dashed line shows the boundary of the Hartmann layer of thickness $\delta_{Ha} = Ha^{-1}$.

wavelength domain length $L_x = 2\pi$ is used in the 3D model. This rather small length has no significant effect on the flow evolution as it has been confirmed in the additional 2D simulations conducted with $L_x = 4\pi$ (shown in figure 8) and $L_x = 2\pi$.

The simulations show that the 3D flow remains Q2D at these values of Ha and Gr . At the same time, its reproduction by the 2D SM82 model is inaccurate in some aspects. The instantaneous distributions of velocity components and temperature shown in figure 8 clearly illustrate the difference. 2D approximations (see figure 8a-c) are similar to 3D flows (see figure 8d-f) in terms of the largest typical streamwise wavelength (about 1.5) but demonstrate noticeably less regular pattern and higher energy in shorter wavelengths. The difference is reflected by the point signals of velocity and temperature shown in figure 9. Comparing figures 9b and 9d, we also see that the 2D approximation substantially underestimates the typical amplitude of velocity fluctuations. As an example, the standard deviation for the signal of u_x in the middle of the duct ($z = 0$) is 0.33 for the 2D model and 0.71 for the 3D model. Computed values of volume-average kinetic energy of the fluctuations (not shown) confirm this conclusion. The values of energy found in the 2D approximation are about an order of magnitude lower than in the actual flow computed in the framework of the 3D model. Interestingly, the misrepresentation of the structure of velocity and temperature fluctuations by the 2D model does not lead to a similarly strong inaccuracy in the prediction of the effect of mixing by fluctuations. Profiles of average streamwise velocity and temperature in figures 8(g, h) show strong change in comparison with the base flow, but only moderate differences between the 2D and 3D results.

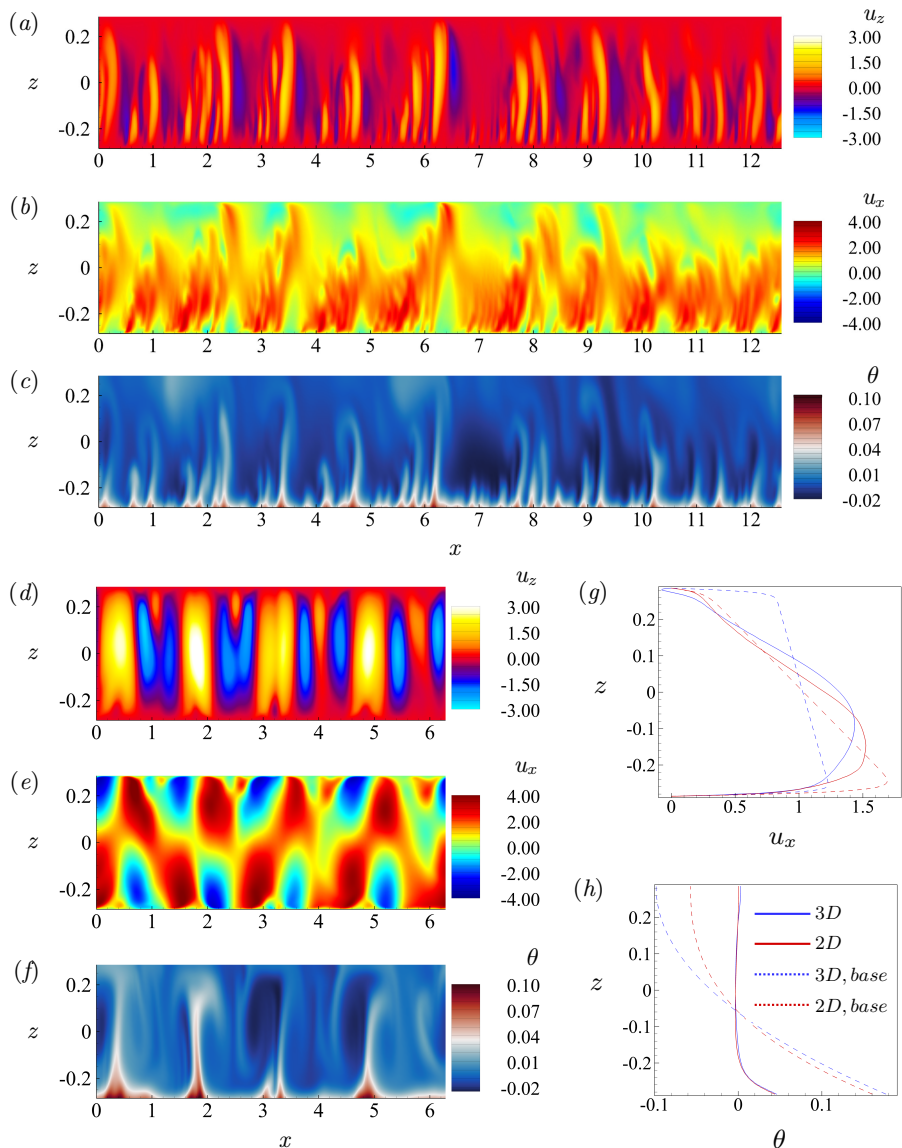


FIGURE 8. Flow structure in nonlinear regime at $Gr = 10^{10}$, $Ha = 10000$. The instantaneous distributions of u_z (a, d), u_x (b, e), and θ (c, f) obtained in 2D and 3D (plotted in the midplane $y = 0$) models are shown in (a)-(c) and (d)-(f), respectively. The profiles of u_x and θ obtained by averaging over x and time (with the base flow profiles from figure 5c, f) are shown, respectively, in (g) and (h).

3.2.4. Applicability of the SM82 model: summary

We conclude that the SM82 approximation accurately represents Q2D flows at moderately large Gr (10^8 and 10^9 in our system). The accuracy deteriorates at higher Gr even though the flow remains Q2D. An example of this is observed at $Ha \gtrsim 4000$ and $Gr = 10^{10}$. The base flow profiles are clearly different between the 2D and 3D models (see figures 5c, f). The 2D linear stability analysis is qualitatively correct in the sense that it correctly predicts the principal type of the unstable perturbations and the streamwise wavelength of the most unstable mode (see figure 6c). The values of the growth rate γ are, however, substantially underestimated by the 2D model (see figure 6c and table 4). The

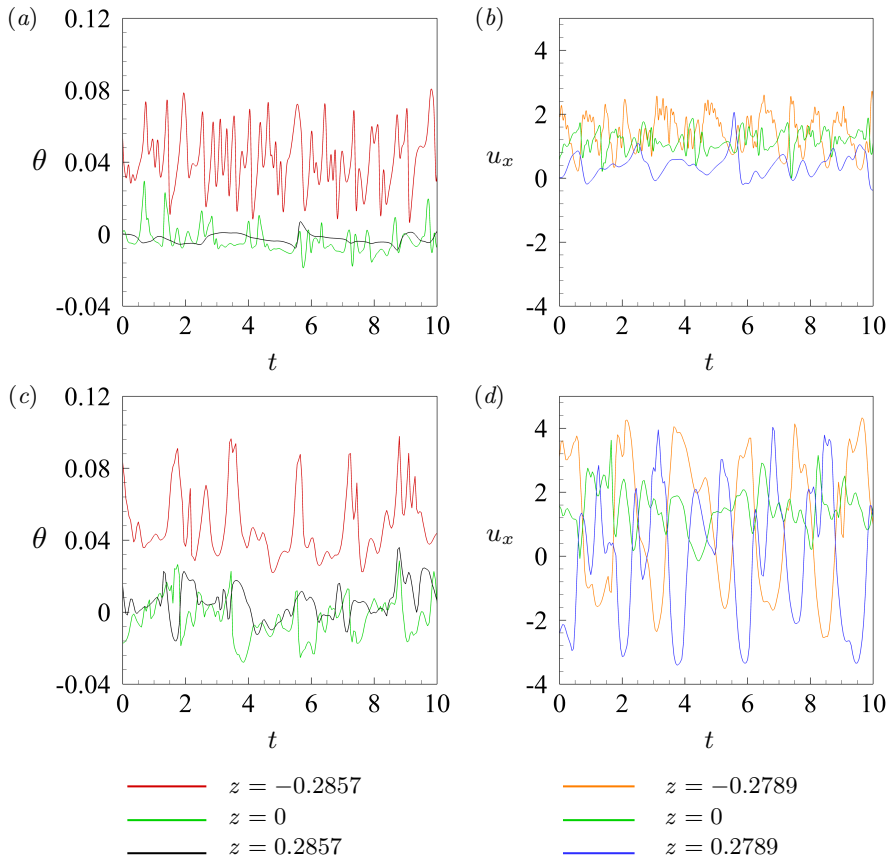


FIGURE 9. Time signals of temperature (a, c) and streamwise velocity (b, d) at $y = 0$ (in the 3D flow) in the nonlinear regime at $Ha = 10^4$, $Gr = 10^{10}$ are shown for 2D (a, b) and 3D (c, d) models.

nonlinear flow states resulting from the instability are predicted incorrectly by the 2D model, which adds artificial irregularity and short-wave fluctuations and underestimates the amplitude of velocity fluctuations (see figures 8 and 9).

We do not have a satisfactory explanation to this effect and leave its further exploration for future studies. It should be mentioned that the quality of the 2D approximation improves with increasing Ha . As an example, the values of the linear instability growth rate γ shown in table 4 are underpredicted by the 2D model by about 35% at $Ha = 4000$ and by about only 18% at $Ha = 10000$.

In the remaining part of this paper, the discussion of the instability and nonlinear states is based on the SM82 2D approximation for flows at $Gr = 10^8$ and 10^9 and on the full 3D solutions for flows at 10^{10} .

3.3. Results of linear stability analysis

The results of the linear stability analysis are summarized in figures 10–12 and table 5. We need to mention that the wavelength λ is varied with step 0.1 in the simulations. The computed values of the exponential growth rate γ as a function of the wavelength λ for various combinations of Ha and Gr are shown in figure 10. Two trends of the linear stability behaviour were proposed by Zhang & Zikanov (2014): (1) a higher growth rate and shorter wavelength appear at higher Gr ; (2) an increase of Ha leads to a higher growth rate. The second, apparently counterintuitive effect was attributed by Zhang &

Gr	Ha	λ_{max}	γ_{max}	Gr	Ha	λ_{max}	γ_{max}	Gr	Ha	λ_{max}	γ_{max}
10^8	1000	0.8	0.487	10^9	1000	—	—	10^{10}	1000	—	—
10^8	2000	0.8	0.465	10^9	2000	0.6	2.671	10^{10}	2000	—	—
10^8	3000	0.9	0.400	10^9	3000	0.6	2.827	10^{10}	3000	—	—
10^8	4000	0.9	0.336	10^9	4000	0.6	2.856	10^{10}	4000	0.4	11.674
10^8	5000	1.0	0.277	10^9	5000	0.6	2.833	10^{10}	5000	0.4	12.023
10^8	6000	1.1	0.226	10^9	6000	0.6	2.786	10^{10}	6000	0.4	12.094
10^8	7000	1.1	0.184	10^9	7000	0.6	2.726	10^{10}	7000	0.4	12.112
10^8	8000	1.2	0.149	10^9	8000	0.6	2.659	10^{10}	8000	0.4	12.106
10^8	9000	1.3	0.120	10^9	9000	0.6	2.589	10^{10}	9000	0.4	12.161
10^8	10000	1.4	0.096	10^9	10000	0.6	2.517	10^{10}	10000	0.4	12.106

TABLE 5. Results of linear stability analysis. Wavelengths λ_{max} and exponential growth rates γ_{max} of the fastest growing modes are shown as functions of Ha and Gr . Only the data for flow regimes identified as Q2D in the analysis of the base flow are shown.

Zikanov (2014) to modification of the base flow, namely to suppression of the transverse circulation resulting in weaker mixing and stronger unstable temperature stratification.

In order to investigate these trends for our system and parameter range, we present the exponential growth rate γ_{max} of the fastest growing modes and the corresponding wavelengths λ_{max} in figure 11 and table 5. Our results are clearly consistent with the first trend, γ_{max} increases and λ_{max} decreases with growing Gr . However, we find a different behaviour in regard of the second trend. The increase of Ha leads to noticeable or slight decrease of the exponential growth rates at $Gr = 10^8$ or $Gr = 10^9$, respectively (see figure 10c). For $Gr = 10^{10}$, γ is nearly insensitive to the values of Ha .

We conclude that the counterintuitive behaviour of stronger instability at higher Ha is not observed in Q2D flows at high Ha considered in our study. It is, nevertheless, noteworthy that γ_{max} does not decrease with Ha at $Gr = 10^{10}$. Increase slightly at $Ha \lesssim 6000$ and remains practically constant at higher Ha . The enhanced friction in the Hartmann boundary layers is compensated by another effect, the only plausible candidate for which is the strong modification of the streamwise velocity profile visible in figure 5c. U_x strongly grows with Ha in the bottom half of the duct, i.e., its part with the strongest unstable temperature gradient.

The findings have critical implications for design and operation of the fusion reactor systems, since they indicate that strength of the convection instability is not diminished by strong magnetic fields at $Gr \geq 10^{10}$ typical for reactor blankets.

The spatial structure of the unstable modes is illustrated in figure 12 for $Gr = 10^8, 10^9, 10^{10}$ and $Ha = 10^4$. The structures are qualitatively similar to those found for Q2D instabilities by Zhang & Zikanov (2014). Consistent with the first trend mentioned above and with the base flow modification illustrated in figure 5 is the fact that the energy of growing perturbations becomes contained to the lower part of the duct at higher values of Gr .

3.4. Results of DNS of nonlinear flows

The results concerning the nonlinear flow regimes are illustrated in figures 8(d, e, f), 13, 14, and 15. DNS approach based on direct solution of the nonlinear governing equations is utilized. The 2D SM82 model (2.13)–(2.15) and the computational domain of length $L_x = 4\pi$ are used for flows at $Gr = 10^8$ and 10^9 . Full 3D equations (2.1)–(2.3) are solved and the domain is reduced to $L_x = 2\pi$ at $Gr = 10^{10}$. Other parameters of computational model are described in section 2.5. Each simulation starts with the streamwise-independent base flow (see section 3.2) computed at the same Gr and Ha , to which

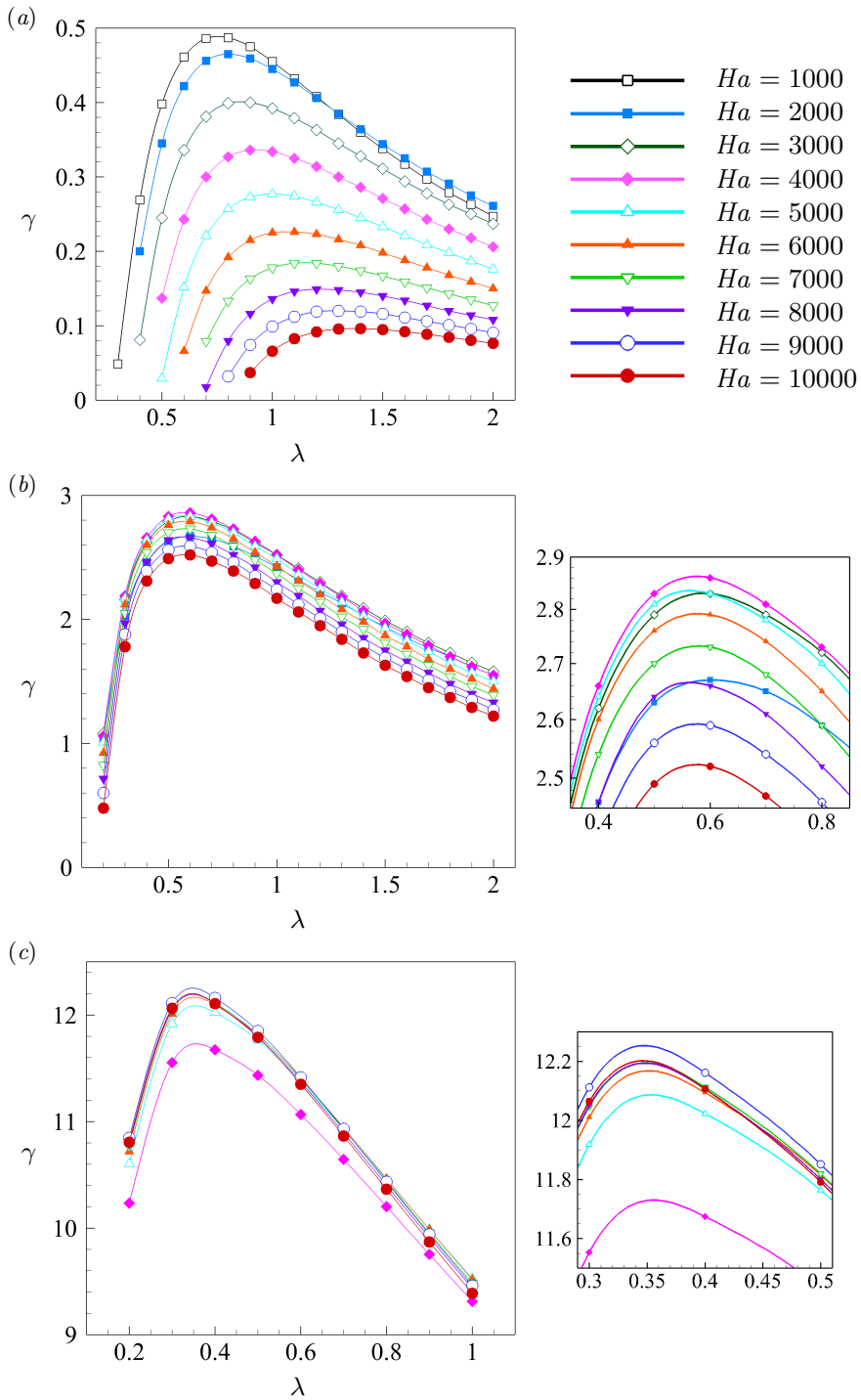


FIGURE 10. Rates of exponential growth γ shown as functions of axial wavelength λ at $Gr = 10^8$ (a), $Gr = 10^9$ (b), and $Gr = 10^{10}$ (c) for various values of Ha . Results of 2D approximation and 3D computational analysis are shown, respectively, for $Gr = 10^8$, 10^9 and $Gr = 10^{10}$. Additional plots in (b) and (c) show zoomed-in areas around $(\lambda_{max}, \gamma_{max})$.

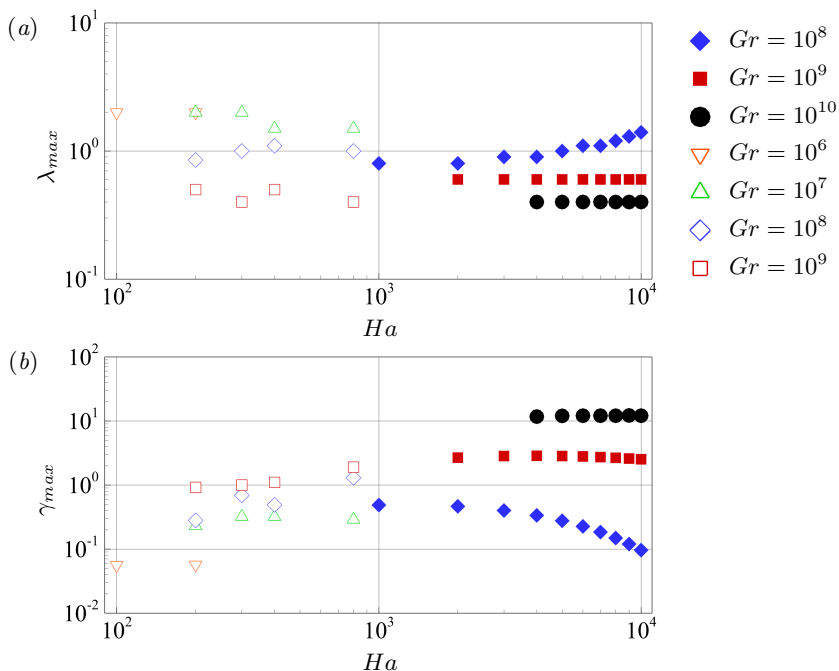


FIGURE 11. The wavelength λ_{max} (a) and the exponential growth rate γ_{max} (b) of the fastest growing perturbations as a function of Ha . The data are taken from table 5. The results of the current work and that of Zhang & Zikanov (2014) are denoted as filled and unfilled elements, respectively. Results of 2D approximation and 3D computational analysis are shown, respectively, for $Gr = 10^8$, 10^9 and $Gr = 10^{10}$.

random small-amplitude ($\sim 10^{-3}$) random perturbations of velocity and temperature are added.

The typical flow evolution is illustrated by the curves of average kinetic energy shown in figure 13. The flow reaches a fully developed state after the instability and initial development. The evolution of the fully developed flow is computed for at least 500 time units for the 2D model at $Gr = 10^8, 10^9$ and at least 100 time units for the 3D model at $Gr = 10^{10}$. At this stage, the integral parameters fluctuate around steady means (at $Gr = 10^9$ and 10^{10}) or remain steady (at $Gr = 10^8$). The amplitudes of the fluctuations are small at $Gr = 10^9$ and large, but still moderate at $Gr = 10^{10}$.

Structure of fully developed flows is illustrated in figures 8 and 14. The velocity field shows finite-amplitude roll-like structures (hereafter referred to as rolls) resulting from the instability, which are superimposed on a streamwise-independent mean flow (see figures 8d and 14a, d). The rolls cause variations of temperature (see figures 8f, 14c and 14f). Transport of the rolls by the mean flow is a known reason of MCFs in horizontal channels (Zikanov *et al.* 2013; Zhang & Zikanov 2014; Zikanov *et al.* 2021).

Comparison of the flow structures in figures 8d-f and 14 reveal the effect of the value of Gr on convection rolls. As anticipated, increase of Gr leads to higher non-dimensional amplitude of the velocity fluctuations. This results in stronger vertical mixing as illustrated by the streamwise- and time-averaged profiles in figure 14g, h. In particular, a nearly uniform vertical distribution of average temperature with a narrow boundary layer at the bottom is observed at $Gr = 10^{10}$.

As we discussed earlier, MCFs caused by the instability have potentially critical implications for design and operation of liquid-metal components of nuclear fusion

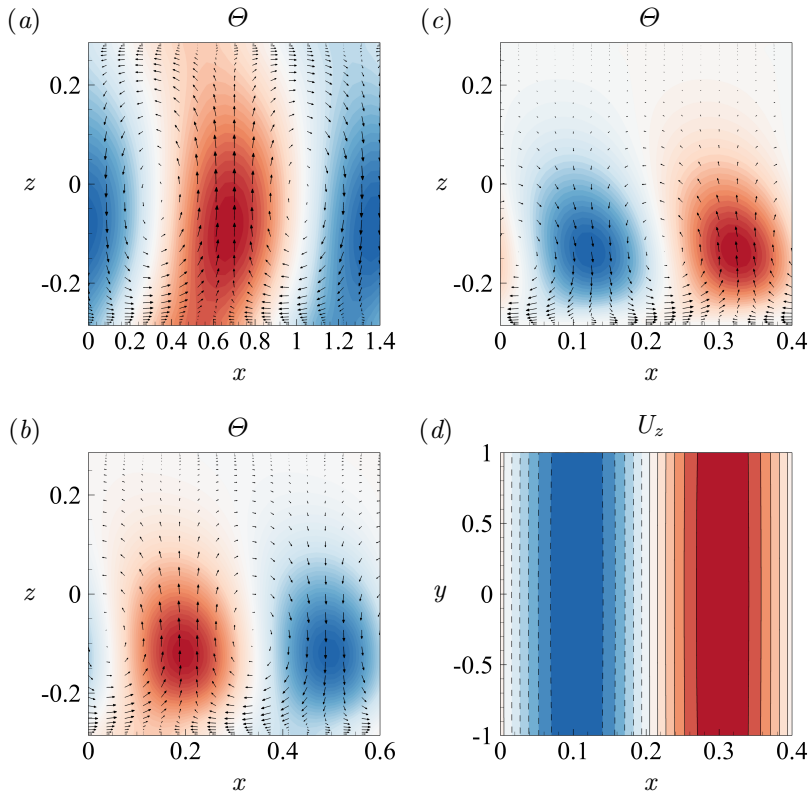


FIGURE 12. Spatial structure of the fastest growing instability modes during the stage of exponential growth at $Gr = 10^8$ (a), $Gr = 10^9$ (b), and $Gr = 10^{10}$ (c),(d) for $Ha = 10000$. Results of 2D approximation and 3D computational analysis are shown, respectively, for $Gr = 10^8, 10^9$ and $Gr = 10^{10}$. Perturbations of temperature and vector fields of velocity perturbations (u' , w') in the vertical midplane ($y = 0$) are shown in (a)-(c). Perturbations of vertical velocity in the horizontal midplane section $z = 0$ are shown in (d). Solid and dashed isolines indicate positive and negative values, respectively.

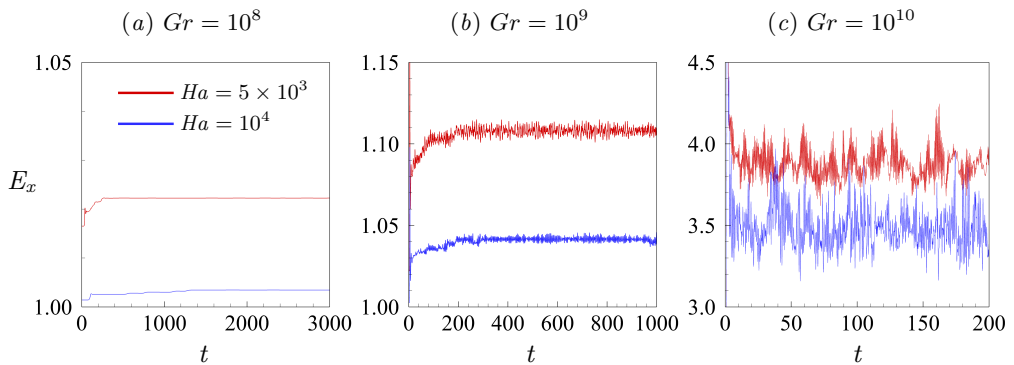


FIGURE 13. Time signals of the kinetic energy of the streamwise velocity obtained in the DNS of flows at $Gr = 10^8$ (a), $Gr = 10^9$ (b), and $Gr = 10^{10}$ (c) for $Ha = 5000$ and $Ha = 10000$. Results of 2D approximation and 3D computational analysis are shown, respectively, for $Gr = 10^8, 10^9$ and $Gr = 10^{10}$.

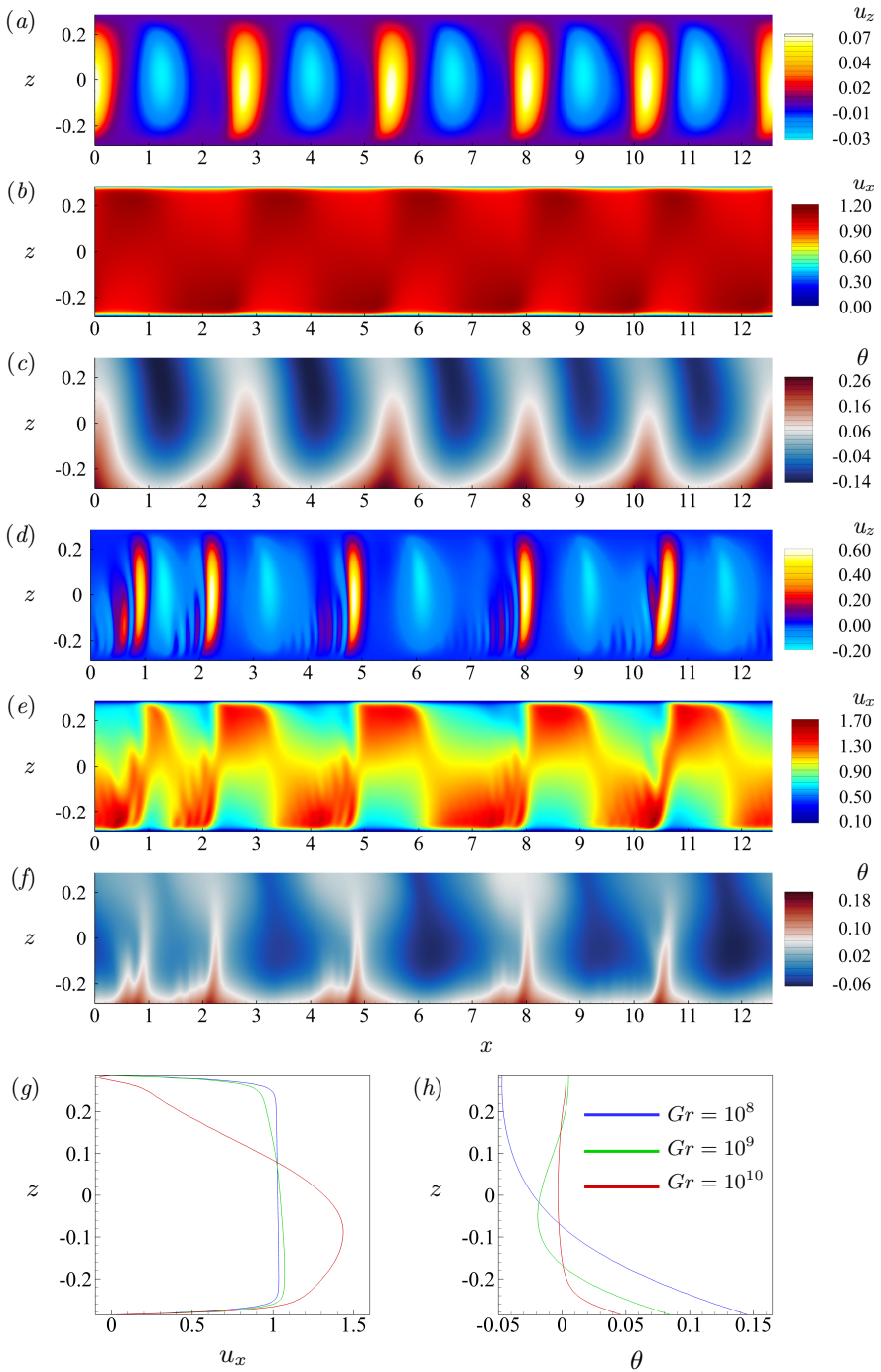


FIGURE 14. Flow structure in nonlinear regime at $Gr = 10^8$ (a-c) and $Gr = 10^9$ (d-f) for $Ha = 10000$. The instantaneous distributions of u_z (a, d), u_x (b, e), and θ (c, f) obtained in the 2D model are shown. The profiles of u_x and θ obtained by averaging over x and time are shown, respectively, in (g) and (h)

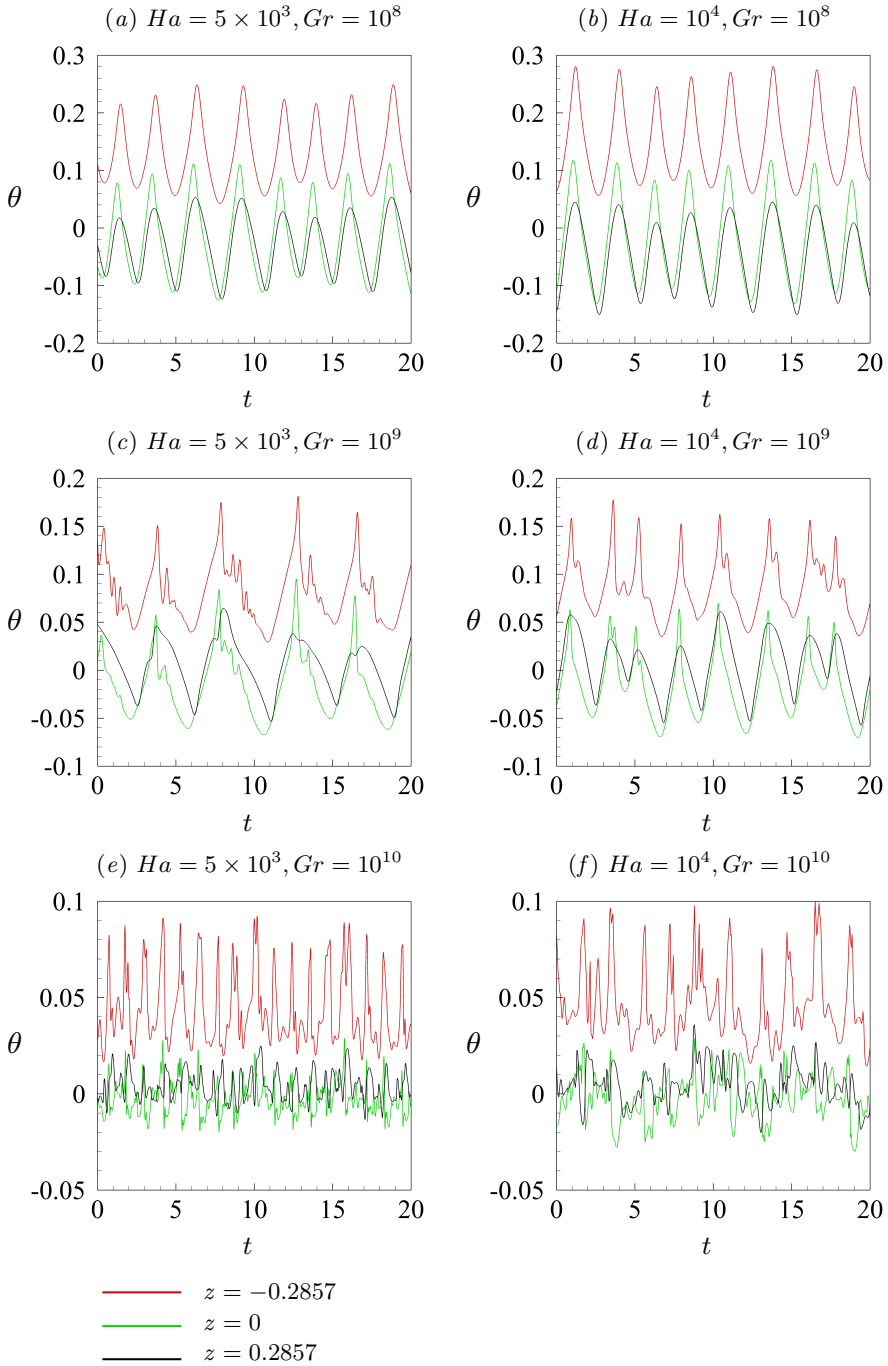


FIGURE 15. Time signals of temperature measured at top and bottom walls and in the middle of the duct in fully developed flows at $Gr = 10^8, 10^9, 10^{10}$ are shown for $Ha = 5 \times 10^3$ in (a, c, e) and for $Ha = 10^4$ in (b, d, f). Results of 2D approximation and 3D computational analysis are shown, respectively, for $Gr = 10^8, 10^9$ (a – d) and $Gr = 10^{10}$ (e – f).

reactors. The DNS results allow us, for the first time, to evaluate the properties of the MCFs at the high values of Gr and Ha corresponding to the actual reactor conditions.

In addition to the instantaneous temperature distributions in figures 8*f*, 14*c* and 14*f*, the discussion will be based on the point-signals of temperature measured at the top and bottom walls and in the middle of the duct (see figure 15). As discussed, e.g., by Zikanov *et al.* (2021), measuring such signals is the most reliable and commonly used tool for studying MCFs in experiments.

The evident conclusion from the DNS data is that MCFs are fully present in flows with $Gr = 10^8, 10^9, 10^{10}$ and the highest values $Ha = 5 \times 10^3$ and 10^4 considered in this study. The fluctuations are observed in the entire duct. The temperature signals are regular and dominated by one or several low frequencies (the typical period is 2-3 non-dimensional time units at $Gr = 10^8$ and 10^9). The signal is less regular and characterized by higher typical frequencies at $Gr = 10^{10}$.

Interestingly, the non-dimensional amplitude of the temperature fluctuations decreases noticeably with growing Gr . Comparison of the signals in the two columns of figure 15 demonstrates that value of Ha has practically no effect on the MCFs.

Considering the practical implications, it is interesting to evaluate the parameters of the MCFs in dimensional units. We will do that for the temperature signals at the bottom of the duct ($z = -0.2857$) assuming the duct half-width $d = 5$ cm and using the physical properties of PbLi at 573 K (Zikanov *et al.* 2021). The wall heat rate is $q = 10.56$ kWm⁻² at $Gr = 10^8$, $q = 105.6$ kWm⁻² at $Gr = 10^9$ and $q = 1056$ kWm⁻² at $Gr = 10^{10}$. We find, by applying the temperature scale qd/κ , that the largest amplitude of fluctuations of wall temperature is in the range 5 – 6 K at $Gr = 10^8$, 44 – 62 K at $Gr = 10^9$, and somewhat unrealistic 180 – 300 K at $Gr = 10^{10}$. The typical time period of the fluctuations is 5.64 s at $Gr = 10^8$, 6.45 s at $Gr = 10^9$, and 4.51 s at $Gr = 10^{10}$ for $Ha = 10^4$.

Similar evaluations have been done for the future experiments on the recently built experimental facility (see, e.g., Belyaev *et al.* 2017), in which liquid mercury flows in the duct with the half-width of $d = 2.8$ cm. The physical properties of Hg are taken at 303 K (Zikanov *et al.* 2021). The wall heat rate is $q = 9.59$ kWm⁻² at $Gr = 10^8$ and $q = 95.9$ kWm⁻² at $Gr = 10^9$. The results of nonlinear simulations allow us to predict the largest amplitude of fluctuations of temperature in the middle of the duct. The amplitudes are in the range of 2 – 3 K at $Gr = 10^8$ and 12 – 18 K at $Gr = 10^9$. The typical time period of the fluctuations is 1.1 s at $Gr = 10^8$ and 1.58 s at $Gr = 10^9$ for $Ha = 1000$.

4. Concluding remarks

We have analysed mixed convection in a liquid metal flow in a duct with bottom heating and transverse magnetic field. The analysis is extended to much higher values of Ha and Gr than the previous analysis of similar effects by Zhang & Zikanov (2014).

The main conclusion of our work is that magnetoconvective fluctuations appear at the parameters anticipated for operational regimes of blankets and divertors of future fusion reactors. The fluctuations are not suppressed or even significantly reduced in amplitude by the very strong magnetic field. The amplitude remains high, reaching tens or hundreds (depending on the value of Gr) K in a typical duct geometry. This has significant far-reaching implications for mixing, heat and mass transfer, and structural integrity of reactor components. The most dangerous modes of the instability have the form of rolls localized in the lower half of the duct and having the streamwise wavelength measured in horizontal half-widths of the duct, approximately, between 0.8 and 1.4 at $Gr = 10^8$, 0.6 at $Gr = 10^9$, and 0.4 at $Gr = 10^{10}$.

Another conclusion concerns applicability of the two-dimensional approximation by Sommeria & Moreau (1982) to flows with thermal convection. We have found that

the approximation may become inaccurate at high values of Gr even though the flow remains quasi-two-dimensional. Reasons of this phenomenon remain to be understood. The conclusion itself, however, is important as a warning against application of the model without a proper verification.

Further study of MCFs at high Hartmann and Grashof numbers is warranted by their practical importance and theoretical significance. Many interesting possible directions of future work can be suggested. We mention two of them. One is the exploration of the phenomenon for other geometries, where strong MCFs are known to exist, for example for downward flow in a vertical duct. Another particularly interesting direction is the analysis of the effects of finite thermal and electrical conductivities of the walls.

Authors are thankful to D. Krasnov for continuing assistance with the numerical model and S. Molokov for interesting and useful discussions. Work of R. Akhmedagaev and O. Zikanov is supported by the US NSF (Grant CBET 1803730 "Extreme magnetoconvection"). Work of Y. Listratov is supported by the Ministry of Science and Education of the Russian Federation (Grant 14.Z50.31.0042) and by the Russian Foundation for Basic Research (Grant NNIO 18-508-12005).

Declaration of Interests. The authors report no conflict of interest.

REFERENCES

- ABDOU, M., MORLEY, N. B., SMOLENTSEV, S., YING, A., MALANG, S., ROWCLIFFE, A. & ULRICKSON, M. 2015 Blanket/first wall challenges and required R&D on the pathway to DEMO. *Fusion Eng. Des.* **100**, 2–43.
- ALBOUSSIÈRE, T., GARANDET, J. P. & MSOREAU, R. 1993 Buoyancy-driven convection with a uniform magnetic field. Part 1. asymptotic analysis. *J. Comp. Phys.* **253**, 545–563.
- BELYAEV, I., IVOCHKIN, Y. P., LISTRATOV, Y. I., RAZUVANOV, N. & SVIRIDOV, V. 2015 Temperature fluctuations in a liquid metal MHD-flow in a horizontal inhomogeneously heated tube. *High Temp.* **53** (5), 734–741.
- BELYAEV, I., SARDOV, P., MELNIKOV, I. & FRICK, P. 2021 Limits of strong magnetoconvective fluctuations in liquid metal flow in a heated vertical pipe affected by a transverse magnetic field. *Int. J. Therm. Sci.* **101**, 106773.
- BELYAEV, I. A., SVIRIDOV, V. G., BATENIN, V. M., BIRYUKOV, D. A., NIKITINA, I. S., MANCHKHA, S. P., PYATNITSKAYA, N. YU., RAZUVANOV, N. G. & SVIRIDOV, E. V. 2017 Test facility for investigation of heat transfer of promising coolants for the nuclear power industry. *Therm. Eng.* **64** (11), 841–848.
- BRANOVER, H. 1978 *Magnetohydrodynamic Flow in Ducts*. New York: Wiley.
- DAVIDSON, P. A. 2016 *Introduction to Magnetohydrodynamics, 2nd Ed.* Cambridge University Press.
- GELFGAT, A. YU. & MOLOKOV, S. 2011 Quasi-two-dimensional convection in a three-dimensional laterally heated box in a strong magnetic field normal to main circulation. *Phys. Fluids* **23**, 034101.
- GELFGAT, A. YU. & ZIKANOV, O. 2018 Computational modeling of magnetoconvection: effects of discretization method, grid refinement and grid stretching. *Comp. Fluids* **175**, 66–82.
- GENIN, L. G., ZHILIN, V. G., IVOCHKIN, Y. P., RAZUVANOV, N. G., BELYAEV, I. A., LISTRATOV, Y. I. & SVIRIDOV, V. G. 2011 Temperature fluctuations in a heated horizontal tube affected by transverse magnetic field. In *Proc. 8th PAMIR Conf. Fund. Appl. MHD*, pp. 37–41. Borgo, Corsica, France.
- KIRILLOV, I.R. & MURAVIEV, E.V. 1997 Review of liquid metal divertor concepts for tokamak reactors. *Fusion Technology* 1996 pp. 251–254.
- KRASNOV, D., ZIKANOV, O. & BOECK, T. 2011 Comparative study of finite difference approaches to simulation of magnetohydrodynamic turbulence at low magnetic Reynolds number. *Comp. Fluids* **50**, 46–59.
- KRASNOV, D., ZIKANOV, O. & BOECK, T. 2012 Numerical study of magnetohydrodynamic duct flow at high Reynolds and Hartmann numbers. *J. Fluid Mech.* **704**, 421–446.
- LISTRATOV, Y. I., OGNERUBOV, D., ZIKANOV, O. & SVIRIDOV, V. 2018 Numerical simulations of mixed convection in liquid metal flow within a horizontal pipe with transverse magnetic field. *Fluid Dyn. Res.* **50** (5), 051407.

- LYUBIMOVA, T. P., LYUBIMOV, D. V., MOROZOV, V. A., SCURIDIN, R. V., HADID, H. B. & HENRY, D. 2009 Stability of convection in a horizontal channel subjected to a longitudinal temperature gradient. Part 1. Effect of aspect ratio and Prandtl number. *J. Fluid Mech.* **635**, 275–295.
- NI, M.-J., MUNIPALLI, R., HUANG, P., MORLEY, N. B. & ABDOU, M. A. 2007 A current density conservative scheme for incompressible MHD flows at a low magnetic Reynolds number. Part I: On a rectangular collocated grid system. *J. Comp. Phys.* **227**, 174–204.
- OZOE, H. 2005 *Magnetic Convection*. Imperial College Press.
- POTHÉRAT, A. 2007 Numerical simulations of an effective two-dimensional model for flows with a transverse magnetic field. *Phys. Fluids* **19** (7), 074104.
- POTHÉRAT, A., SOMMERIA, J. & MOREAU, R. 2000 An effective two-dimensional model for MHD flows with transverse magnetic field. *J. Fluid Mech.* **424**, 75–100.
- POTHÉRAT, A., SOMMERIA, J. & MOREAU, R. 2005 Numerical simulations of an effective two-dimensional model for flows with a transverse magnetic field. *J. Fluid Mech.* **534**, 155–143.
- SAHU, S., COURTESSOLE, C., RANJAN, A., BHATTACHARYAY, R., SKETCHLEY, T. & SMOLENTSEV, S. 2020 Thermal convection studies in liquid metal flow inside a horizontal duct under the influence of transverse magnetic field. *Phys. Fluids* **32** (6), 067107.
- SMOLENTSEV, S., MOREAU, R. & ABDOU, M. 2008 Characterization of key magnetohydrodynamic phenomena for PbLi flows for the US DCLL blanket. *Fusion Eng. Des.* **83**, 771–783.
- SMOLENTSEV, S., MOREAU, R., BÜHLER, L. & MISTRANGELO, C. 2010 MHD thermofluid issues of liquid-metal blankets: Phenomena and advances. *Fusion Eng. Des.* **85** (7-9), 1196–1205.
- SMOLENTSEV, S., VETCHA, N. & MOREAU, R. 2012 Study of instabilities and transitions for a family of quasi-two-dimensional magnetohydrodynamic flows based on a parametrical model. *Phys. Fluids* **24**, 024101.
- SOMMERIA, J. & MOREAU, R. 1982 Why, how and when MHD-turbulence becomes two-dimensional. *J. Fluid Mech.* **118**, 507–518.
- DE LES VALLS, E. MAS, SEDANO, L., BATET, L., RICAPITO, I., AIELLO, A., GASTALDI, O. & GABRIEL., F. 2008 Lead–lithium eutectic material database for nuclear fusion technology. *J. Nucl. Mater.* **376**, 353–357.
- VETCHA, N., SMOLENTSEV, S., ABDOU, M. & MOREAU, R. 2013 Study of instabilities and quasi-two-dimensional turbulence in volumetrically heated magnetohydrodynamic flows in a vertical rectangular duct. *Phys. Fluids* **25** (2), 024102.
- VO, T., POTHÉRAT, A. & SHEARD, G. J. 2017 Linear stability of horizontal, laminar fully developed, quasi-two-dimensional liquid metal duct flow under a transverse magnetic field and heated from below. *Phys. Rev. Fluids* **2**, 033902.
- ZHANG, X. & ZIKANOV, O. 2014 Mixed convection in a horizontal duct with bottom heating and strong transverse magnetic field. *J. Fluid Mech.* **757**, 33–56.
- ZHANG, X. & ZIKANOV, O. 2017 Thermal convection in a toroidal duct of a liquid metal blanket. part ii. effect of axial mean flow. *Fusion Eng. Des.* **116**, 40–46.
- ZHANG, X. & ZIKANOV, O. 2018 Convection instability in a downward flow in a vertical duct with strong transverse magnetic field. *Phys. Fluids* **30**, 117101.
- ZHAO, Y. & ZIKANOV, O. 2012 Instabilities and turbulence in magnetohydrodynamic flow in a toroidal duct prior to transition in Hartmann layers. *J. Fluid Mech.* **692**, 288–316.
- ZIKANOV, O. 2019 *Essential Computational Fluid Dynamics, 2nd Ed.* Wiley.
- ZIKANOV, O., KRASNOV, D., BOECK, T., THESS, A. & ROSSI, M. 2014 Laminar-turbulent transition in magnetohydrodynamic duct, pipe, and channel flows. *Appl. Mech. Rev.* **66** (3), 030802.
- ZIKANOV, O., LISTRATOV, Y., RAZUVANOV, N., BELYAEV, I., FRICK, P. & SVIRIDOV, V. 2021 Mixed convection in pipe and duct flows with strong magnetic fields. *Appl. Mech. Rev.* **73** (1), 010801.
- ZIKANOV, O., LISTRATOV, YA. & SVIRIDOV, V. G. 2013 Natural convection in horizontal pipe flow with strong transverse magnetic field. *J. Fluid Mech.* **720**, 486–516.